

Spring 2009

Bathymetric uncertainty model for the L-3 Klein 5410 sidescan sonar

Marc Stanton Moser

University of New Hampshire, Durham

Follow this and additional works at: <https://scholars.unh.edu/thesis>

Recommended Citation

Moser, Marc Stanton, "Bathymetric uncertainty model for the L-3 Klein 5410 sidescan sonar" (2009). *Master's Theses and Capstones*. 451.

<https://scholars.unh.edu/thesis/451>

This Thesis is brought to you for free and open access by the Student Scholarship at University of New Hampshire Scholars' Repository. It has been accepted for inclusion in Master's Theses and Capstones by an authorized administrator of University of New Hampshire Scholars' Repository. For more information, please contact nicole.hentz@unh.edu.

**BATHYMETRIC UNCERTAINTY MODEL
FOR THE L-3 KLEIN 5410 SIDESCAN SONAR**

BY

**MARC STANTON MOSER
B.S. Oregon State University, 1994**

THESIS

**Submitted to the University of New Hampshire
In Partial Fulfillment of
The Requirements for the Degree of**

**Master of Science
In
Ocean Engineering**

May, 2009

UMI Number: 1466942

INFORMATION TO USERS

The quality of this reproduction is dependent upon the quality of the copy submitted. Broken or indistinct print, colored or poor quality illustrations and photographs, print bleed-through, substandard margins, and improper alignment can adversely affect reproduction.

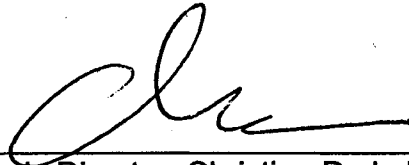
In the unlikely event that the author did not send a complete manuscript and there are missing pages, these will be noted. Also, if unauthorized copyright material had to be removed, a note will indicate the deletion.

UMI[®]

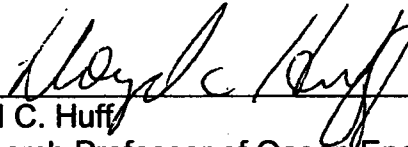
UMI Microform 1466942
Copyright 2009 by ProQuest LLC
All rights reserved. This microform edition is protected against
unauthorized copying under Title 17, United States Code.

ProQuest LLC
789 East Eisenhower Parkway
P.O. Box 1346
Ann Arbor, MI 48106-1346

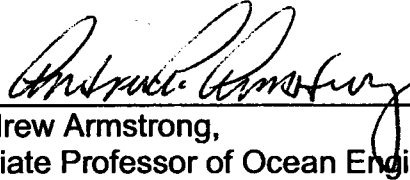
This thesis has been examined and approved.




Thesis Director, Christian P. de Moustier,
Professor of Electrical and Computer Engineering and
Ocean Engineering



Lloyd C. Huff
Research Professor of Ocean Engineering



Andrew Armstrong,
Affiliate Professor of Ocean Engineering



Brian R. Calder
Research Associate Professor of Electrical and
Computer Engineering and Ocean Engineering

April 2, 2009
Date

TABLE OF CONTENTS

LIST OF FIGURES	iv
LIST OF TABLES.....	vii
ABSTRACT.....	viii
INTRODUCTION	1
CHAPTER 1 OVERVIEW.....	2
1.1 L-3 Klein 5410 description	2
1.2 Previous work with uncertainty	3
1.3 Benefits of bathymetric uncertainty model.....	4
CHAPTER 2 ANGLES AND OFFSETS	5
2.1 Offsets, coordinate systems and rotations.....	5
2.2 Vertical offsets.....	7
2.3 Launch angle determination	11
2.4 Ray tracing	12
2.5 Angle of incidence on the seafloor	19
CHAPTER 3 UNCERTAINTY	23
3.1 Uncertainty calculations.....	23
3.2 Calculation of observed difference data	35
3.3 Mean difference between 5410 soundings and reference surface	37
3.4 Effect of signal-to-noise ratio (SNR)	44
3.5 Time resolution (pulse bandwidth).....	46
3.6 5410 Signal Processing.....	49
3.7 Angular Uncertainty.....	50
CHAPTER 4 RESULTS	55
CHAPTER 5 EVALUATION OF UNCERTAINTY MODEL WITH OCEAN MAPPING STANDARDS	62
CHAPTER 6 CONCLUSIONS AND FUTURE WORK	70
6.1 Summary	70
6.2 Suggestions for future work.....	71
LIST OF REFERENCES.....	74
APPENDIX A LIST OF TERMS	80
APPENDIX B UNCERTAINTY SCENARIO	82
APPENDIX C UNCERTAINTY VALUES.....	83
APPENDIX D COMMENTS ON SOUND SPEED PROFILE VARIABILITY	84
APPENDIX E SONAR EQUATIONS.....	86
APPENDIX F PLOT OF MAGNITUDE OUTPUT (SINGLE LINE).....	88
APPENDIX G NARRATIVE OF MAJOR POINTS.....	90

LIST OF FIGURES

Figure 1: R/V Coastal Surveyor offsets	6
Figure 2: Tait-Bryan rotation sequence showing yaw (a), pitch (b), and roll (c)....	6
Figure 3: Vertical position of sonar calculated from: (a) static draft, (b) dynamic draft, (c) heave, (d) and (e) induced heave	8
Figure 4: Solution for corrected angle of arrival through law of sines for tetrahedra where the corrected angle of arrival (θ_{Corr}) is AOB, pitch (Γ) is AOC, the raw angle of arrival and roll ($\theta_{\text{raw}} + \Psi$) is COB. OAB, OAC, OCB, and ACB are right angles.	12
Figure 5: Constant negative sound speed gradient layer ray trace.....	15
Figure 6: Constant sound speed ray tracing solution for partial layer.....	17
Figure 7: Zero gradient layer ray trace	18
Figure 8: Azimuth angles for port and starboard rays.....	21
Figure 9: Angle of incidence components for ray vector (a), surface normal (b), and resulting angle of incidence (c).....	22
Figure 10: Difference between corrected angle of arrival (θ_{Corr}), absolute bearing (θ_{Bearing}), and athwartships bearing component (θ_{est})	27
Figure 11: Uncertainty tree (After Hare, et al. (1995) and Calder (2006)). Uncertainties not being displayed include cross-terms for yaw uncertainty and heave, roll and pitch uncertainty on refraction, and heave uncertainty on refraction	29
Figure 12: Total vertical uncertainty and individual uncertainties at 2σ without sonar uncertainties at 20-m altitude	35
Figure 13: Determination of vertical difference between sounding and grid node using the grid resolution (γ) to determine the maximum search radius (r_{max}) for finding the nearest grid node for each sounding	36
Figure 14: Sample mean (black dots) and standard deviation (blue pluses) for 51 lines binned in 0.5° sectors without filtering shows difference data irregularities. Port data is on the left and starboard data is on the right.....	38
Figure 15: Mean filter results for individual lines. Horizontal axis is the line number and the vertical axis is angle from nadir. The color is based on the filter value in meters. Note that the starboard data on the right show peaks around 46° and 65°	39
Figure 16: Sample mean (black dots) and standard deviation (blue pluses) for 51 lines binned in 0.5° sectors with filtering. Port data on the left and starboard data on the right	40
Figure 17: Histograms of de-trended difference data for a single angular bin for 51 lines for gravel (a), sand (b), and bedrock (c) where the red line is the Gaussian fit	41
Figure 18: Multipath noise sources: desired signal path (black line), interference paths (red lines). Inset: pair of receivers separated by a distance of d	42

Figure 19: Bottom and surface multipath angle calculation showing surface and bottom angles. Bottom noise distance (s_{BN}) and surface noise distance (s_{SN}) equals signal path distance (s_{signal}). Bottom noise angle (θ_{BN}) and signal noise angle (θ_{SN}) is a function of sensor depth (z_{sensor}), depth (z) and signal distance.....	43
Figure 20: Noise source vs signal source for 5-m and 20-m depths assuming a sensor depth of one meter and zero sound speed gradient	44
Figure 21: Probability density function (pdf) of phase difference error from equation (95) for source at bore sight, (70°), noise from surface reflection (117°) at different SNR from equation (103). Decreases in SNR result in the mean of the pdf shifting towards the noise solution and increasing standard deviation	45
Figure 22: Probability density functions of phase error for three different element spacing from equation (95) where the source is at boresight (70°), phase for each pair shown with the black line, and noise from surface reflection (117°), phase for each pair shown with the red line.....	45
Figure 23: Theoretical effect of pulse bandwidth on the swath area sonified and the vertical measurement.....	47
Figure 24: Histogram of depth difference data for single angular sector (69.75° to 70.25°).....	51
Figure 25: Histogram of estimated angular error for single angular sector (69.75° to 70.25°).....	52
Figure 26: Estimated angular uncertainty assuming all observed uncertainties are the result of the sonar angular uncertainty	53
Figure 27: Calculated angular uncertainty for gravel (a), sand (b), and bedrock (c), for data without multipath negative sound speed gradient artifacts.....	56
Figure 28: Calculated angular uncertainty for negative gradient multipath for gravel (a) and sand (b)	58
Figure 29: Calculated angular uncertainty for gravel (a), sand (b), and bedrock (c) by angle of incidence on the seafloor	59
Figure 30: Extrapolated angular uncertainty model based on data acquired over sand showing the original data (squares) along with the model data (points and pluses).....	60
Figure 31: Top figure showing surface depth for single ping. Bottom figure showing total vertical uncertainties at 2σ for single ping showing exported CARIS HIPS, and calculated angular uncertainty model results with observed uncertainty	61
Figure 32: Theoretical total vertical uncertainty for ideal 5410 for altitudes of 5-m and 20-m showing null at nadir and IHO standards for each depth.....	62
Figure 33: Theoretical vertical uncertainty for a 5410 with a DC bias. Neither depth range meets IHO Special Order, and only a portion of the swath meets IHO Order 2.....	64
Figure 34: Theoretical total vertical uncertainty at 15-m altitude for ideal 5410 with Applanix POS M/V 320 using DGPS correctors (a), Applanix POS M/V 320 using RTK (b), and Applanix POS M/V Elite with improved sound speed profile conditions (c) showing range in predicted performance to IHO Order 1	

standards out to 66 m for (a), IHO Order 1 out to 71 m for (b), and IHO Order 1 out to 81 m for (c)	66
Figure 35: Reduced uncertainty tree for fixed sonar (After Hare, et al. (1995) and Calder (2006))	72
Figure 36: Sound speed cast compilation where the DOY of the cast is shown in the graph at a depth of 30 m	84
Figure 37: Sound speed, temperature, and salinity of casts. Deepest points of each salinity and temperature profiles were extrapolated	85
Figure 38: Acoustic backscatter negative sound speed profile gradient multipath interference for the starboard side out to 100 m. The left is nadir and the right is the farthest away from the sonar. The wavy structures to the right are due to interference, (DOY 213 in Figure 36)	85
Figure 39: Receive beam pattern correction (from Glynn, 2007)	87
Figure 40: Flowchart of proposed processing steps to solve for sonar uncertainties using multibeam echosounder (MBES) data as a reference surface.....	91

LIST OF TABLES

Table 1: Sidescan line spacing based on range scale and coverage	67
Table 2: Maximum speed for complete bathymetric coverage.....	69

ABSTRACT

BATHYMETRIC UNCERTAINTY MODEL FOR THE L-3 KLEIN 5410 SIDESCAN SONAR

By

Marc Stanton Moser

University of New Hampshire, May, 2009

The L-3 Klein 5410 sidescan sonar system acquires acoustic backscatter imagery and bathymetry data. A bathymetry uncertainty model was developed for this sonar to predict its performance against hydrographic standards set by the International Hydrographic Organization (IHO). Elements of the model not specific to this sonar were adapted from existing uncertainty models, and the remainder was calculated by comparing the 5410 bathymetry with a reference surface obtained from multibeam echosounder data. The sonar's angular uncertainty was solved for different bottom types with best results obtained over sandy bottoms, where, after removal of some system biases, the bathymetry met standards for hydrographic surveys Order 1 from 30° to 75° from nadir. The model predicts that the total propagated uncertainty at 20-m altitude meets IHO standards over a swath width equal to seven times the water-depth, with a central gap one water-depth wide for an ideal 5410.

INTRODUCTION

The problem:

The L-3 Klein 5410 is one of a number of phase differencing sonars (PDS) manufactured by different vendors and used for seafloor mapping. Whether called interferometric [1-6], bathymetric sidescan [7-18], multi-angle swath bathymetry [19, 20], phase measuring sidescan [21], phase interferometry [22], or phase differencing sonar [23], these sonars have the common attribute of using one or more pairs of receivers to measure the phase difference of an incoming bottom return to calculate the angle of arrival and two-way travel time. Although these systems share some basic characteristics with widely used multibeam echosounders and sidescan sonars, differences in the way a depth measurement is determined mean that bathymetric uncertainty models specific to multibeam echosounders are not necessarily representative of the uncertainty from PDS.

Overall goals:

- a) Evaluate vertical sounding uncertainty for all sources but 5410 sonar uncertainties
- b) Compare calculated with observed 5410 vertical uncertainty
- c) Derive a 5410 uncertainty model from residual uncertainties
- d) Evaluate the 5410 uncertainty model against seafloor mapping specifications

CHAPTER 1

OVERVIEW

1.1 L-3 Klein 5410 description

The L-3 Klein 5410 phase differencing sonar (PDS) is a modified version of the popular L-3 Klein series 5000 sidescan sonar, which is used in many seafloor mapping activities. The addition of two receive and one synthetic (created from four sidescan array elements) bathymetry elements on each side enables the 5410 to acquire bathymetry [14]. The measured echo phase and magnitude from the bathymetry element pairs allow the calculation of range and angle of arrival estimates, which together are used to calculate depth and depth position. The system as studied used a continuous wave (CW) pulse at two different pulse duration settings and is now known as a “version 1” of this 5410 sonar.

The acoustic backscatter imagery from the L-3 Klein 5000 series has a 0.20–0.36 m along track and 0.075–0.300 m across track resolution [24]. This resolution meets the International Hydrographic Organization (IHO) feature detection criteria for a one meter cubic object [25] provided the sonar is operated to maximize feature detection.

The analyzed 5410 is jointly owned by the National Oceanic and Atmospheric Administration (NOAA) Office of Coast Survey (OCS) and National Marine Fisheries Service (NMFS). Personnel at the University of New Hampshire (UNH) Center for Coastal and Ocean Mapping / Joint Hydrographic Center (CCOM/JHC) have been working with the 5410 for a number of years. A method to convert the raw SDF formatted data into a format usable by CARIS HIPS software as well as a calibration procedure developed by Glynn [14] enabled the bathymetry of the 5410 to be used for seafloor mapping. Separately from CCOM/UNH, Zerr et al. [26] also acquired and processed 5410 bathymetry for rapid environment assessment. CARIS HIPS is a commercially available package to process hydrographic data [27], specifically seafloor mapping data used primarily for nautical charting and safety of navigation purposes. In this project, a timing method described by Calder and McLeod [28] was also utilized for improved data acquisition. A proof of concept survey in New York Harbor was successfully completed in late 2006 [13]. Newer versions of the processing code were developed by James Glynn, Christian de Moustier, and Brian Locke in 2007 and 2008.

1.2 Previous work with uncertainty

The total uncertainty for the bathymetric solution of the 5410 can be broken into two parts: sonar specific uncertainty and uncertainty from every other source. The uncertainty from every other source has been investigated and described by Hare, et al. [29, 30]. Theoretical PDS uncertainties including

the effects of shifting foot print [11, 12, 19], baseline decorrelation [11, 12, 19], multipath and ambient noise [8, 16], and volume reverberation [7] have also been explored. In general, these theoretical PDS uncertainties have a detrimental effect on the angle of arrival solution. Other sonar specific uncertainties also include the impact of processing methods on the angle of arrival solution and the uncertainties associated with the sonar characteristics including pulse duration, acoustic frequency, pulse type, and the effect of environmental conditions on the angle of arrival solution.

Performance and uncertainties for sonar bathymetry have been evaluated for non 5410 PDS systems. Gostnell et al. [5, 31] evaluated the bathymetry from a Geoacoustics Geoswath, a SEA Swath Plus, and a Teledyne Benthos 3D. Hogarth [32] derived an uncertainty model for the Geoacoustics Geoswath. Hiller et al. [33] examined modifying the Combined Uncertainty and Bathymetry Estimator (CUBE) for use with PDS bathymetry.

1.3 Benefits of bathymetric uncertainty model

The primary benefit of a bathymetric uncertainty model for the 5410 is to enable potential users to determine whether the system meets certain criteria for seafloor mapping. Other benefits of a 5410 uncertainty model include pre-survey planning and bathymetric data processing. Calder and Mayer [34] developed a method to process large bathymetric data sets utilizing uncertainty (CUBE). An uncertainty model for the 5410 bathymetry would allow the use of CUBE for processing 5410 data.

CHAPTER 2

ANGLES AND OFFSETS

Before discussing the uncertainty equations it is necessary to define the source and definition of major components used in those calculations. Sonar systems are composed of several sensing components that are typically separated from each other on the moving echosounding platform. Clear definitions of offsets and rotations between components are needed to utilize the attitude output from the motion sensor, while the methodology for ray tracing and angle of incidence calculations are important for the uncertainty calculations and later analysis.

2.1 Offsets, coordinate systems and rotations

Offsets are described using the three axis system shown in Figure 1. The Y offset is positive forward, the X offset is positive to starboard, and the Z offset is positive down (into the water) in this context. X, Y, and Z offsets are the measured distances from the top of the IMU center mark to the phase center of each sonar transducer. Rotations around these axes are defined using the right-hand coordinate system conventions.

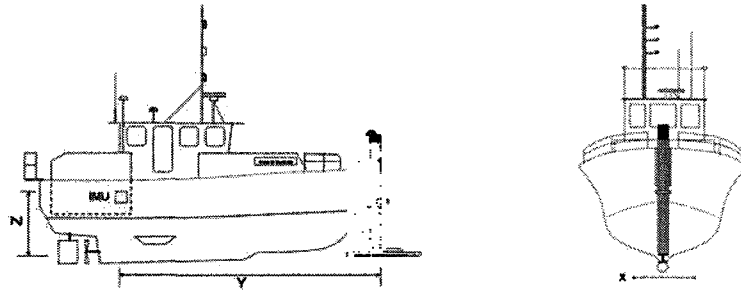


Figure 1: R/V Coastal Surveyor offsets

Attitude data were acquired using a rotation convention called Tait-Bryan [35, 36]. The sequence for Tait-Bryan rotations is yaw-pitch-roll (Φ, Γ, Ψ). A positive rotation around the Z axis is clockwise. A positive rotation around the Y axis is port up. A positive rotation around the X axis is bow up. An example Tait-Bryan sequence is shown Figure 2, with positive yaw, pitch, and roll rotations.

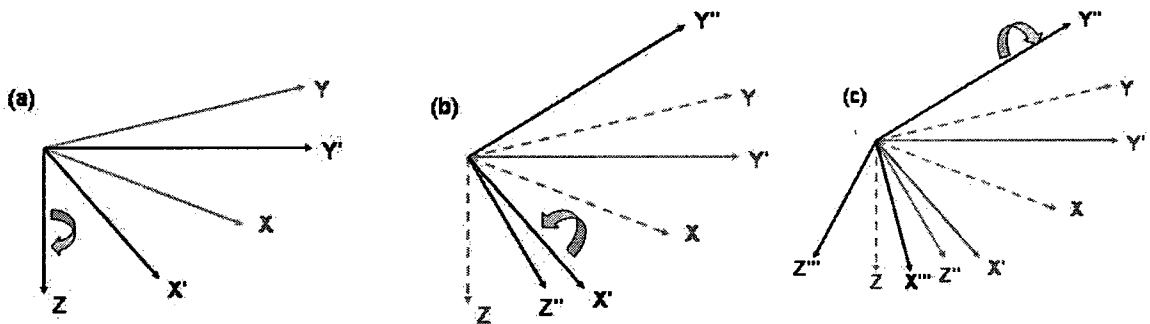


Figure 2: Tait-Bryan rotation sequence showing yaw (a), pitch (b), and roll (c)

The Tait-Bryan sequence can be used with rotation matrices to describe and quantify the position of the sonar at any given time. Goldstein [37] derives the matrices to describe these rotations.

$$R(\Psi) = \begin{pmatrix} 1 & 0 & 0 \\ 0 & \cos \Psi_{att} & -\sin \Psi_{att} \\ 0 & \sin \Psi_{att} & \cos \Psi_{att} \end{pmatrix} \quad (1)$$

$$R(\Gamma) = \begin{pmatrix} \cos \Gamma_{att} & 0 & \sin \Gamma_{att} \\ 0 & 1 & 0 \\ -\sin \Gamma_{att} & 0 & \cos \Gamma_{att} \end{pmatrix} \quad (2)$$

$$R(\Phi) = \begin{pmatrix} \cos \Phi_{att} & -\sin \Phi_{att} & 0 \\ \sin \Phi_{att} & \cos \Phi_{att} & 0 \\ 0 & 0 & 1 \end{pmatrix} \quad (3)$$

2.2 Vertical offsets

For ray tracing, the vertical position of the sensor transducer with respect to the water surface at the time of reception (z_{sensor}) is calculated using the total heave (H), the static draft (D_s), dynamic draft (D_d), and the vertical offset of the sensor to the reference point (Z), which are illustrated in Figure 3. Static draft is the vertical offset of the reference point (in this case the attitude sensor) to the water surface when the vessel is underway but not making way (i.e. drifting, not moored). Dynamic draft is the vertical offset of the reference point to the water surface when the vessel is underway and making way. Most vessels have a dynamic draft that depends on their speed through the water. The vertical offset (Z) is the measured vertical offset from the attitude sensor (top of the IMU) to the phase center of the sonar. Total heave is a combination of measured heave at

the attitude sensor and induced heave. Measured heave is the vertical movement of the attitude sensor. Induced heave is the apparent vertical movement of the sonar with respect to the attitude sensor due to vessel rotations. The sensor vertical position is used for ray tracing, reduced depth calculation and uncertainty calculations.

$$z_{sensor} = Z - Ds + Dd + H \quad (4)$$

Another vertical change not directly measured or applied is the change in vessel vertical position under different loading conditions. These include using or taking on fresh water, ballast, fuel, passengers, and equipment. Normally these changes would be taken into account with frequent static draft measurements.

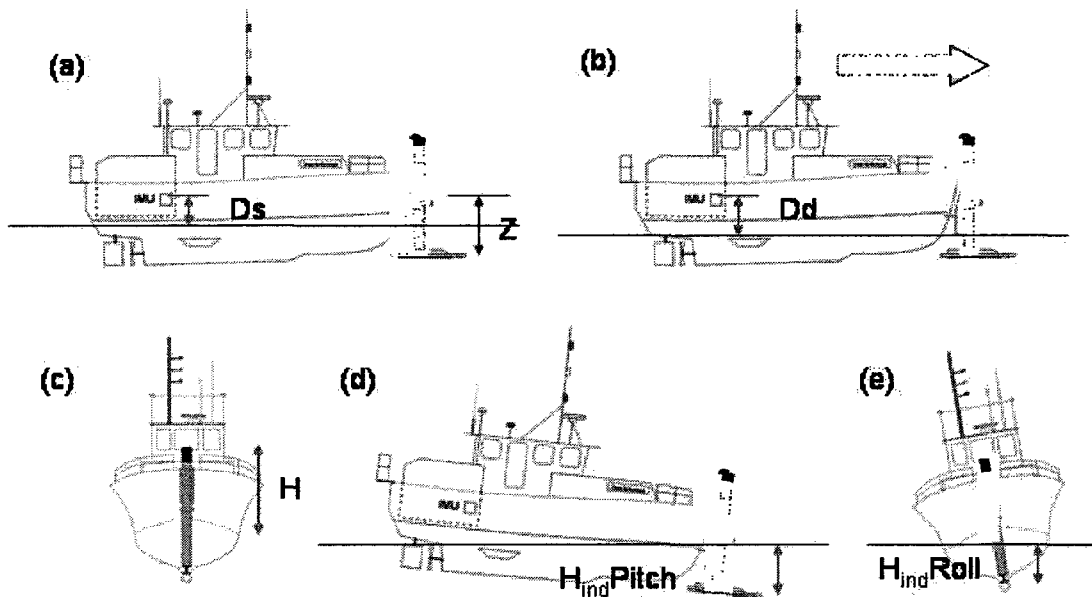


Figure 3: Vertical position of sonar calculated from: (a) static draft, (b) dynamic draft, (c) heave, (d) and (e) induced heave

The rotational matrices can be reduced to calculate a sonar position for a given set of angles. When the rotation matrices are multiplied with a vector of offsets, the result is the rotated sonar position as shown by Hare, et al. [29]. The rotations assume that the rotated body is rigid and there is no flexing or change of the offsets during the rotation.

$$R(\Phi)R(\Gamma)R(\Psi) \begin{bmatrix} Y \\ X \\ Z \end{bmatrix} = \begin{bmatrix} Y_{Rot} \\ X_{Rot} \\ Z_{Rot} \end{bmatrix} \quad (5)$$

Since yaw (Φ) is irrelevant for the calculation of induced heave, the Yaw rotation matrix becomes an identity matrix.

$$\begin{pmatrix} 1 & 0 & 0 \\ 0 & 1 & 0 \\ 0 & 0 & 1 \end{pmatrix} \begin{pmatrix} \cos \Gamma & 0 & \sin \Gamma \\ 0 & 1 & 0 \\ -\sin \Gamma & 0 & \cos \Gamma \end{pmatrix} \begin{pmatrix} \cos \Psi & -\sin \Psi & 0 \\ \sin \Psi & \cos \Psi & 0 \\ 0 & 0 & 1 \end{pmatrix} \begin{bmatrix} Y \\ X \\ Z \end{bmatrix} = \begin{bmatrix} Y_{Rot} \\ X_{Rot} \\ Z_{Rot} \end{bmatrix} \quad (6)$$

The rotation matrices can further be reduced to solve for induced heave. Induced heave is calculated using Pitch (Γ_{att}), Roll (Ψ_{att}), and offsets of the sensor from the attitude sensor (X, Y, Z) [29]:

$$H_{ind} = [-Y \sin(\Gamma_{att}) + X \sin(\Psi_{att}) \cos(\Gamma_{att}) + Z (1 - \cos(\Psi_{att}) \cos(\Gamma_{att}))] \quad (7)$$

Total heave (H) includes the heave at the attitude sensor (H_{att}) and the induced heave resulting from the motion of the vessel (H_{ind}).

$$H = H_{att} + H_{ind} \quad (8)$$

The measured depth (z) and sensor depth (z_{sensor}) and give the depth of water at the time of acquisition. The water depth at time of acquisition can further be reduced to a common vertical datum. Reduction of water depths to a common datum are necessary for comparison of depth data acquired at different

times. The most common vertical datum for NOAA nautical charts is mean lower low water (MLLW), which was used for the test data. Tide measurements (Tides) from the NOAA tide gauges used for this analysis were relative to MLLW.

$$z_{red} = z_{sensor} + z - Tides \quad (9)$$

Since most data were acquired away from the NOAA tide gauges it was necessary to utilize tide zoning to approximate the tides at the geographic location of acquisition. Simple tide zones generated by NOAA for previous hydrographic surveys were used for the tide zoning [38]. The total tide correction was designed to match as closely as possible with the method used by CARIS HIPS [27] so comparison of depth results and surfaces exported from CARIS HIPS would reflect as closely as possible the results calculated independently. Although more advanced methods of tide correction have been developed [39], these methods were not used for this analysis.

The vessel position was evaluated for each ping to determine in which tide zone polygon it resided. Each tide zone polygon was attributed with a range and time corrector. Measured tide data were then corrected for the time and multiplied by the range ratio for the final tide correction, which is consistent with NOAA's hydrographic survey procedures. Tide data from NOAA gauges in Portsmouth, NH (842-3898) and Portland, ME (841-8150) were used.

Although the Portsmouth, NH, tide gauge is very close to the survey area and would have been preferable for all data, it was inoperative for a period of time during data acquisition and the Portland gauge was used for a portion of the data. This should not affect the validity of results.

2.3 Launch angle determination

Since the raw angle of echo arrival reported by the 5410 is with respect to the sonar reference frame, the angle must be converted to an angle with respect to vertical for ray tracing in the water column. The launch angle of a given ray is determined using the raw angle of arrival (θ_{Raw}) with respect to the sonar reference frame, measured roll and pitch, and biases. The angle of arrival is measured from vertical with a value of zero at nadir, -90° to port and 90° to starboard. Pitch (Γ) and roll (Ψ) angles are a combination of the measured values (Γ_{att}, Ψ_{att}) at the attitude sensor and their respective bias ($\Gamma_{bias}, \Psi_{bias}$). The angle of arrival is measured at the instant when the transmitted sound has made a round trip to the bottom and attitude values are evaluated at the arrival time.

$$\Gamma = \Gamma_{att} - \Gamma_{bias} \quad (10)$$

$$\Psi = \Psi_{att} - \Psi_{bias} \quad (11)$$

Using the law of sines for tetrahedra, the corrected angle of arrival (θ_{Corr}) can be calculated using the raw angle of arrival (θ_{Raw}), pitch (Γ), and roll (Ψ). All of the triangles of the tetrahedron are right triangles and four of the angles (Γ , $(90^\circ - \Gamma)$, $(\theta + \Psi)$, $(90^\circ - (\theta + \Psi))$) are known. With the notation given in Figure 4, the law of sines states:

$$\sin \widehat{OAB} \sin \widehat{OBC} \sin \widehat{OCA} = \sin \widehat{OAC} \sin \widehat{OCB} \sin \widehat{OBA} \quad (12)$$

Where $\widehat{OAB} = 90^\circ$, $\widehat{OBC} = 90^\circ - (\theta_{Raw} + \Psi)$, $\widehat{OCA} = 90^\circ - \Gamma$, $\widehat{OAC} = 90^\circ$, $\widehat{OCB} = 90^\circ$ and $\widehat{OBA} = 90^\circ - \theta_{Corr}$. Equation (12) becomes:

$$\sin 90^\circ \sin 90^\circ \sin(90^\circ - \theta_{Corr}) = \sin 90^\circ \sin(90^\circ - (\theta_{Raw} + \Psi)) \sin(90^\circ - \Gamma) \quad (13)$$

Reducing equation (13) results in the solution for the corrected angle of arrival:

$$\sin(90^\circ - \theta_{Corr}) = \sin(90^\circ - (\theta_{Raw} + \Psi)) \sin(90^\circ - \Gamma) \quad (14)$$

$$\cos(\theta_{Corr}) = \cos(\theta_{Raw} + \Psi) \cos(\Gamma) \quad (15)$$

$$\theta_{Corr} = \cos^{-1} [\cos(\Gamma) \cos(\theta_{Raw} + \Psi)] \quad (16)$$

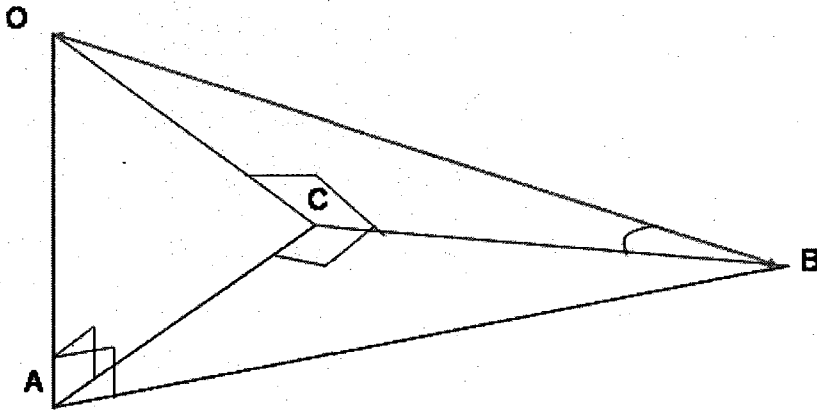


Figure 4: Solution for corrected angle of arrival through law of sines for tetrahedra where the corrected angle of arrival (θ_{Corr}) is AOB, pitch (Γ) is AOC, the raw angle of arrival and roll ($\theta_{raw} + \Psi$) is COB. OAB, OAC, OCB, and ACB are right angles.

2.4 Ray tracing

Echosounding pulses from the 5410 travel obliquely through the water column. The speed at which sound travels through water column varies with depth. The depth, traveled range, and horizontal range are calculated using either a constant sound speed gradient method [40] or a zero gradient method. To match the application method used in CARIS HIPS [27], sound speed profiles were selected based on the time difference between the sound speed cast and the survey line and the distance of the cast to the line. The cast nearest in

distance and time (within three hours) was selected. Most casts acquired for this project have a first entry at around one meter depth. Each cast was extrapolated to the surface for ray tracing using a pressure only gradient. Another option, that consists of extrapolating from the slope of the profile deeper than one meter was not used based on the assumption that the top one meter of the water column would be relatively well mixed.

Cast data also have a finite measured depth. The last measured point is extrapolated to the seafloor by the NOAA cast processing software Velocwin [41] using the 'most probable slope algorithm' method. This Velocwin extrapolated point is at times not deep enough for all rays, so an additional point is generated in Matlab using an isothermal gradient (0.017 s^{-1}) to a depth known to be greater than the maximum survey area depth.

Using the extended cast data, ray tracing for each solution is calculated, depending on the measured sound speed gradient, using either the constant gradient solution or zero gradient solution. The corrected angle of arrival at receive (θ_{Corr}) is evaluated at the measured sensor depth ($z_{\text{sensor}}(\text{Rx})$) at the time of arrival. Subsequently, the average sensor depth between transmit (Tx) and receive (Rx) is used to determine the sensor depth (z_{sensor}) in equation (9).

$$z_{\text{sensor}} = \frac{z_{\text{sensor}}(\text{Tx}) + z_{\text{sensor}}(\text{Rx})}{2} \quad (17)$$

For simplicity, the depth increments in the sound speed cast are used for all but the final layer for layer calculations. A layer is a horizontal slice of the ocean with a constant vertical gradient, assuming that there is no horizontal sound speed gradient. The gradient (g_i) for a given layer is calculated using the

difference in the top and bottom depths of the layer (Δz_i) and the difference in the speed of sound at the top (c_i) and bottom (c_{i+1}) of the layer.

$$g_i = \frac{(c_{i+1} - c_i)}{\Delta z_i} \quad (18)$$

If the gradient does not approach zero, the constant sound speed gradient solution is used to solve for the ray path. The ray parameter, or Snell's Law constant of the ray (p) is given by the corrected angle at receive (θ_{Corr}) and the speed of sound at the sensor (c_{sensor}) [40]. This ray parameter is constant for the entire ray path and is derived using Snell's Law.

$$p = \frac{\sin(\theta_{\text{Corr}})}{c_{\text{sensor}}} = \frac{\sin \theta_2}{c_2} = \frac{\sin \theta_i}{c_i} = \frac{\sin \theta_{i+1}}{c_{i+1}} \quad (19)$$

The radius of curvature (R_i) for a given layer is given from the ray parameter (p) and gradient (g_i) in that layer. The radius of curvature is constant while the gradient is constant.

$$R_i = \frac{1}{p(g_i)} \quad (20)$$

The angle of incidence for the top layer (θ_i) and bottom layer (θ_{i+1}) are calculated using Snell's law, the speed of sound at the sensor (c_{sensor}), top of layer (c_i) and bottom of layer (c_{i+1}).

$$\theta_i = \sin^{-1} \left[\sin(\theta_{\text{Corr}}) \left(\frac{c_i}{c_{\text{sensor}}} \right) \right] = \sin^{-1} [p(c_i)] \quad (21)$$

$$\theta_{i+1} = \sin^{-1} \left[\sin(\theta_{\text{Corr}}) \left(\frac{c_{i+1}}{c_{\text{sensor}}} \right) \right] = \sin^{-1} [p(c_{i+1})] \quad (22)$$

The horizontal distance traveled by the ray (r_{hi}) shown in Figure 5 is given by the ray parameter (p), gradient (g_i), speed of sound at the top of the layer (c_i), and depth difference of the layer (Δz_i).

$$r_{hi} = \frac{\sqrt{1 - [p(c_i + \Delta z_i(g_i))]^2} - \sqrt{1 - (p(c_i))^2}}{p(g_i)} \quad (23)$$

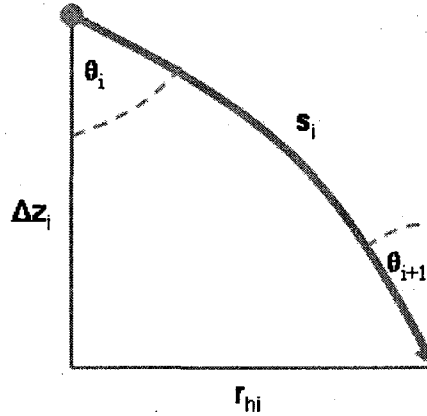


Figure 5: Constant negative sound speed gradient layer ray trace

The distance traveled by the ray (s_i) is given by the radius of curvature (R_i) and the difference in angle of incidence in radians from the top (θ_i) and bottom (θ_{i+1}) of the layer:

$$s_i = R_i(\theta_{i+1} - \theta_i) \quad (24)$$

The travel time of the ray (t_i) through layer i is given by the gradient (g_i), sound speed at the top of the layer (c_i), depth difference of the layer (Δz_i), and the ray parameter (p).

$$t_i = \frac{1}{g_i} \left[\frac{(c_i + g_i \Delta z_i)(1 + \sqrt{1 - (p(c_i))^2})}{c_i(1 + \sqrt{1 - [p(c_i + g_i \Delta z_i)]^2})} \right] \quad (25)$$

As an iterative process, the sum of the travel times through each layer is evaluated against one half of the total recorded two-way travel time (t_f).

$$\text{If } \frac{t_f}{2} - \sum_{i=1}^N t_i > 0 \text{ then continue to next full layer} \quad (26)$$

$$\text{Else } \frac{t_f}{2} - \sum_{i=1}^N t_i < 0 \text{ then evaluate from last full layer} \quad (27)$$

The remaining component of the solution is to solve for the partial layer, where the ray hits the bottom between depth increments of the sound speed profile. The sum of travel times (t_i) up to the last full layer ($N-1$) is subtracted from half the recorded two way travel time ($t_f/2$) for the remaining time (t_r).

$$t_r = \frac{t_f}{2} - \sum_{i=0}^{N-1} t_i \quad (28)$$

The remaining travel time (t_r) is then used to solve the angle of incidence at the bottom (θ_r) using the gradient of the final layer (g_N), and the angle of incidence at the top of the layer (θ_{N-1}).

$$t_r = \frac{1}{g_N} \ln \left[\frac{\tan(\theta_r / 2)}{\tan(\theta_{N-1} / 2)} \right] \quad (29)$$

Therefore,

$$\theta_r = 2 \tan^{-1} \left[\tan(\theta_{N-1} / 2) e^{t_r g_N} \right] \quad (30)$$

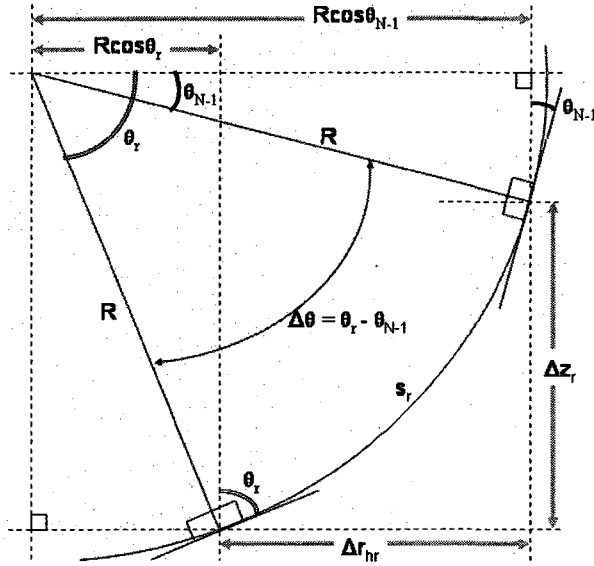


Figure 6: Constant sound speed ray tracing solution for partial layer

The remaining horizontal distance (r_{hr}) can then be solved using the radius of curvature (R_N), and the angle of incidence of the top (θ_{N-1}) and bottom (θ_r) of the partial layer in radians.

$$r_{hr} = R_N [\cos(\theta_{N-1}) - \cos(\theta_r)] \quad (31)$$

The remaining distance traveled (s_r) is solved using the radius of curvature (R), and the angle of incidence of the top (θ_{N-1}) and bottom (θ_r) of the partial layer in radians to calculate the arc distance.

$$s_r = R_N [\theta_r - \theta_{N-1}] \quad (32)$$

The remaining depth difference (Δz_r) is solved using the radius of curvature (R_N), angles of incidence at the top (θ_{N-1}) and bottom (θ_r):

$$\Delta z_r = R [\sin \theta_r - \sin \theta_{N-1}] \quad (33)$$

If the gradient is very small in layer i , the gradient (g_i) approaches zero and the radius of curvature (R_i) approaches infinity. Under these circumstances, the constant sound speed gradient solution cannot be used and the zero gradient

solution must be used. Then the horizontal distance (r_{hi}) traveled by the ray is given by the depth difference (Δz_i) and angle of incidence (θ_i):

$$r_{hi} = \Delta z_i \tan(\theta_i) \quad (34)$$

The distance traveled (s_i) is given by the depth difference (Δz_i) and angle of incidence (θ_i):

$$s_i = \frac{\Delta z_i}{\cos(\theta_i)} \quad (35)$$

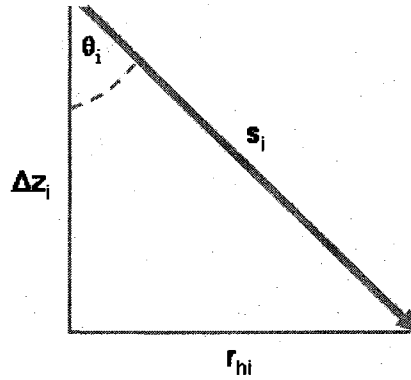


Figure 7: Zero gradient layer ray trace

The travel time (t_i) is given by the depth difference (Δz_i), sound speed (c_i) and angle of incidence (θ_i).

$$t_i = \left(\frac{\Delta z_i}{\cos(\theta_i)} \right) / c_i \quad (36)$$

As with the constant sound speed gradient method, remaining time (t_r) is used to solve for the remaining partial layer. The depth difference (Δz_r) is calculated using the angle of incidence (θ_{N-1}), remaining travel time (t_r), and sound speed (c_{N-1}).

$$\Delta z_r = \cos(\theta_{N-1}) c_{N-1} t_r \quad (37)$$

The remaining horizontal distance is calculated using the depth difference (Δz_r) and angle of incidence (θ_{N-1}).

$$r_{hr} = \Delta z_r \tan(\theta_r) \quad (38)$$

The remaining distance traveled (s_r) is calculated using the depth difference (Δz_r) and angle of incidence (θ_{N-1}).

$$s_r = \frac{\Delta z_r}{\cos(\theta_{N-1})} \quad (39)$$

For all of the layers traveled by the ray, the sums of the travel times ($t_{i:N-1} + t_r$), distance traveled ($s_{i:N-1} + s_r$), layer thickness ($\Delta z_{i:N-1} + \Delta z_r$), and horizontal distance ($r_{h\ i:N-1} + r_{hr}$) provide the final solutions for total distance traveled (s), horizontal range (r_h), and depth below the sensor (z).

2.5 Angle of incidence on the seafloor

The angle of incidence of a ray on the seafloor can be used in the depth uncertainty equations and can also be used to determine the existence of any angle of incidence dependence in the 5410 depth uncertainty. The calculation of the angle of incidence uses the angle of impact (angle of incidence before bottom slope correction) of a given ray to a hypothetical horizontal bottom using Snell's Law and the slope of the bathymetric surface at the point of impact, expressed using the surface normal and the ray vector [42]. For a given surface $f(N, E, z) = 0$, where Northing (N), Easting (E), and depth (z) are

provided, the surface normal and direction cosines can be calculated for that surface as follows:

Each component of the normal vector can be broken down using the partial derivatives of the surface function f .

$$\vec{u} = \left[\frac{\partial f}{\partial N}, \frac{\partial f}{\partial E}, \frac{\partial f}{\partial z} \right] \quad (40)$$

The direction cosines of the normal vector (L_u, M_u, N_u) are calculated from the normalized individual components (N, E, z) of \vec{u} .

$$L_u = \frac{u_N}{|u|} \quad (41)$$

$$M_u = \frac{u_E}{|u|} \quad (42)$$

$$N_u = \frac{u_z}{|u|} \quad (43)$$

Where $|u|$ is the norm of \vec{u} :

$$|u| = \sqrt{u_N^2 + u_E^2 + u_z^2} \quad (44)$$

For a given ray, where the azimuth angle and final angle of incidence with respect to a hypothetical horizontal bottom are provided, the direction cosines of the ray vector \vec{v} can be calculated.

The azimuth of a ray vector is calculated from the vessel heading (Φ) and a corrector. Since these rays are pointing towards (not away) from the source, the resultant azimuth angle for port (Φ_{port}) and starboard (Φ_{stbd}) are reversed.

$$\Phi_{port} = \Phi + 90^\circ \quad (45)$$

$$\Phi_{stbd} = \Phi + 270^\circ \quad (46)$$

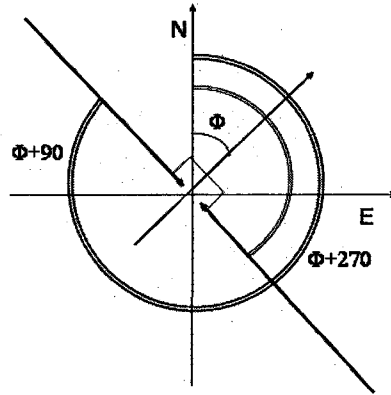


Figure 8: Azimuth angles for port and starboard rays

The azimuth (Φ_{port} and Φ_{stbd}) and initial angle of incidence (θ_{init}) of each ray are used to calculate the normal for the ray.

$$v_E = |v| \sin \theta_{init} \sin \Phi \quad (47)$$

$$v_N = |v| \sin \theta_{init} \cos \Phi \quad (48)$$

$$v_z = |v| \cos \theta_{init} \quad (49)$$

Where $|v|$ is used to normalize the results to calculate the direction cosines (L_v ,

M_v , and N_v) for the ray vector.

$$|v| = \sqrt{v_E^2 + v_N^2 + v_z^2} \quad (50)$$

$$L_v = \frac{v_N}{|v|} \quad (51)$$

$$M_v = \frac{v_E}{|v|} \quad (52)$$

$$N_v = \frac{v_z}{|v|} \quad (53)$$

The final angle of incidence (θ_{Inc}) is calculated by using the surface normal \vec{u} and ray vector \vec{v} .

$$\theta_{inc} = \cos^{-1} \left[\frac{u_N v_N}{|u||v|} + \frac{u_E v_E}{|u||v|} + \frac{u_z v_z}{|u||v|} \right] \quad (54)$$

Equation (54) can be expressed as the inner product of normal vectors shown in equation (55).

$$\theta_{inc} = \cos^{-1} \left[(\vec{u} \cdot \vec{v}) / (|\vec{u}||\vec{v}|) \right] \quad (55)$$

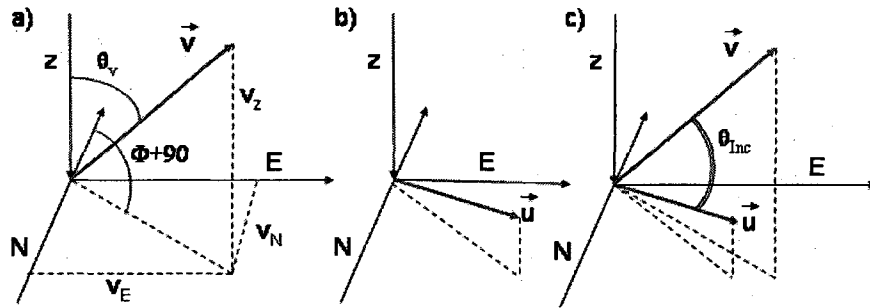


Figure 9: Angle of incidence components for ray vector (a), surface normal (b), and resulting angle of incidence (c)

CHAPTER 3

UNCERTAINTY

Chapter 2 defined the basic building blocks for the values utilized in the uncertainty equations. With these definitions the total propagated uncertainty can now be calculated for 5410 data. Once the uncertainties for all but the sonar are calculated and the difference data of the 5410 and multibeam reference surface are calculated, the 5410 uncertainty model can be calculated.

3.1 Uncertainty calculations

Uncertainty calculations for all uncertainty with the exception of the sonar were derived from the equations documented from Hare, et al. [29, 30]. These equations were appropriate for the 5410 analysis since the components of the uncertainty equations appeared to match those of the processing software [27] used to create the bathymetric surfaces in this analysis, allowing for a direct comparison of calculated uncertainty values against a known standard.

3.1.1 Discussion on uncertainty values used

Uncertainty values used were either directly obtained from vendor specifications, laboratory testing, or best estimates based on available information. Uncertainty values provided by the vendors included those uncertainties associated with vessel motion and positioning [43, 44] and sonar

characteristics [45]. Some uncertainty values for those sonar characteristics not provided by the vendor were observed from laboratory testing by Glynn [14]. The remaining non-sonar uncertainties were estimated from observations and guidance from relevant standards [3, 23, 25].

This analysis uses baseline sound speed and tide uncertainty values that are lower than recommended by NOAA specifications [3, 23], because observed uncertainties were less than the uncertainties calculated by CARIS HIPS. Uncertainties for draft were also estimated and the resulting baseline values are lower than recommended by NOAA. The uncertainty values used in the Matlab code written for this analysis were the same as those used in CARIS HIPS for every uncertainty except for the 5410 uncertainties. A listing of uncertainty values used in both applications is shown in Appendix C.

Multibeam echosounder biases are normally resolved for time, pitch, yaw and roll. It should be noted that the only practical bias that could be resolved with the 5410 data used here were roll bias values. Since there are no data at nadir, solving for pitch and navigation time delay biases is difficult. Due to the very precise timing system used during acquisition, timing uncertainties were assumed to be minimal. Yaw was also difficult to solve since the data acquired for the purpose of solving for that bias were degraded due to negative sound speed gradient multipath artifacts. Therefore, other bias values including yaw and navigation time were not solved but were assumed to be zero. As discussed by Hughes Clark [46], a misalignment around the z axis of the roll and pitch axes of the attitude sensor would result in cross talk between measured roll and pitch

values. This cross talk would be visible as a heave artifact. Since yaw is not being included in these calculations, the links between yaw, pitch, roll, and induced heave will not be discussed further.

3.1.2 Uncertainty propagation

The method for uncertainty propagation considered here is based on a Taylor Series expansion of the multivariate uncertainty function [46, 47]. The uncertainty for a function $j = F(k, l)$ composed of two independent and random variables (k, l) can be described as the sum of products of the squared partial derivatives and variances of each variable.

$$\sigma_j^2 = \left(\frac{\partial j}{\partial k}\right)^2 \sigma_k^2 + \left(\frac{\partial j}{\partial l}\right)^2 \sigma_l^2 \quad (56)$$

If the two variables (k, l) are not independent, then an additional term (covariance) must also be considered as part of the total uncertainty equation.

$$\sigma_j^2 = \left(\frac{\partial j}{\partial k}\right)^2 \sigma_k^2 + \left(\frac{\partial j}{\partial l}\right)^2 \sigma_l^2 + 2\left(\frac{\partial j}{\partial k}\right)\left(\frac{\partial j}{\partial l}\right)\sigma_{kl} \quad (57)$$

Where σ_{kl} is the covariance of k and l.

Based on the uncertainty equations from Hare, et al. [29, 30], it was assumed that all of the uncertainty calculations can be used for the 5410 data with the exception of the depth/sonar equations which are system specific.

3.1.3 Range and Bearing estimation

Since the angle of arrival and total range for each ray (calculated from ray tracing) are not usually the straight line bearing and range used in the uncertainty model by Hare, et al. [29, 30], it is necessary to compute the corresponding

estimated straight line bearing ($\theta_{bearing}$) and range (r_{est}). The straight line bearing can be calculated using the horizontal range (r_h) and depth (z).

$$\theta_{bearing} = \tan^{-1} \left[\frac{r_h}{z} \right] \quad (58)$$

Since the straight line bearing is the result of pitch and across track components, the bearing must be broken into separate pitch and across track components to use the uncertainty equations described by Hare, et al. [29, 30]. Using equation (16) and the estimated straight line bearing and pitch, the estimated athwartships component of the straight line bearing can be calculated.

$$\theta_{est} = \cos^{-1} \left[\frac{\cos \left(\tan^{-1} \left[\frac{r_h}{z} \right] \right)}{\cos(\Gamma)} \right] \quad (59)$$

The r_h used to calculate the bearing should not be confused with the Cartesian coordinates used for the offsets. The horizontal range (r_h) as used in equation (59) and shown in Figure 10 is a directionless value and does not correspond with the usual definitions of x and y as across and along track components of a ray tracing solution or Easting and Northing position coordinates.

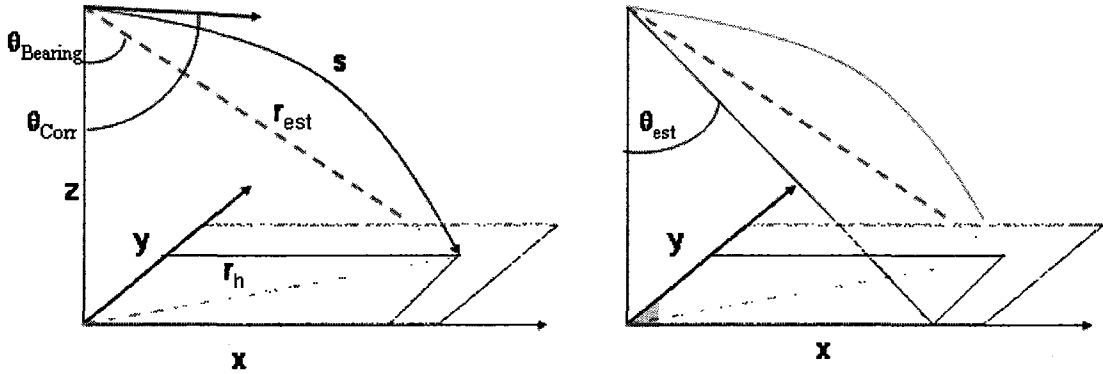


Figure 10: Difference between corrected angle of arrival (θ_{Corr}), absolute bearing (θ_{Bearing}), and athwartships bearing component (θ_{est})

$$r_{\text{est}} = \sqrt{r_h^2 + z^2} \quad (60)$$

The effective straight line sound speed for each ray (c_{est}) can be calculated from the measured two-way travel time (t_f) and estimated straight path range (r_{est}).

$$c_{\text{est}} = \frac{r_{\text{est}}}{(t_f / 2)} \quad (61)$$

Assuming that the difference between the combination of pitch and estimated bearing ($\cos(\Gamma)\cos(\theta_{\text{est}})$) and the corrected angle of arrival (θ_{Corr}) is small, the depth uncertainties associated with the estimated bearing should be equal to the depth uncertainties associated with the corrected angle of arrival.

3.1.4 Non-sonar uncertainty equations

The critical path for 5410 depth uncertainty analysis is highlighted in red in Figure 11. Using the observed difference data as a proxy for the reduced depth and measured depth uncertainties, the uncertainty equations can be reversed to calculate the desired sonar characteristics. Besides the direct relationships

between uncertainty components, possible correlation (covariance terms) are illustrated using dashed lines. This diagram and the following equations are meant to address only those sources of uncertainty specific to this data set and do not address other sources of uncertainty associated with some multibeam echosounders (i.e. uncertainty due to beam steering). Other sources of uncertainty, which are not specifically addressed, include the effect of yaw uncertainty on pitch and roll and the ultimate effect on heave [46]. Other possible sources of uncertainty correlation will be addressed with the specific uncertainty equations.

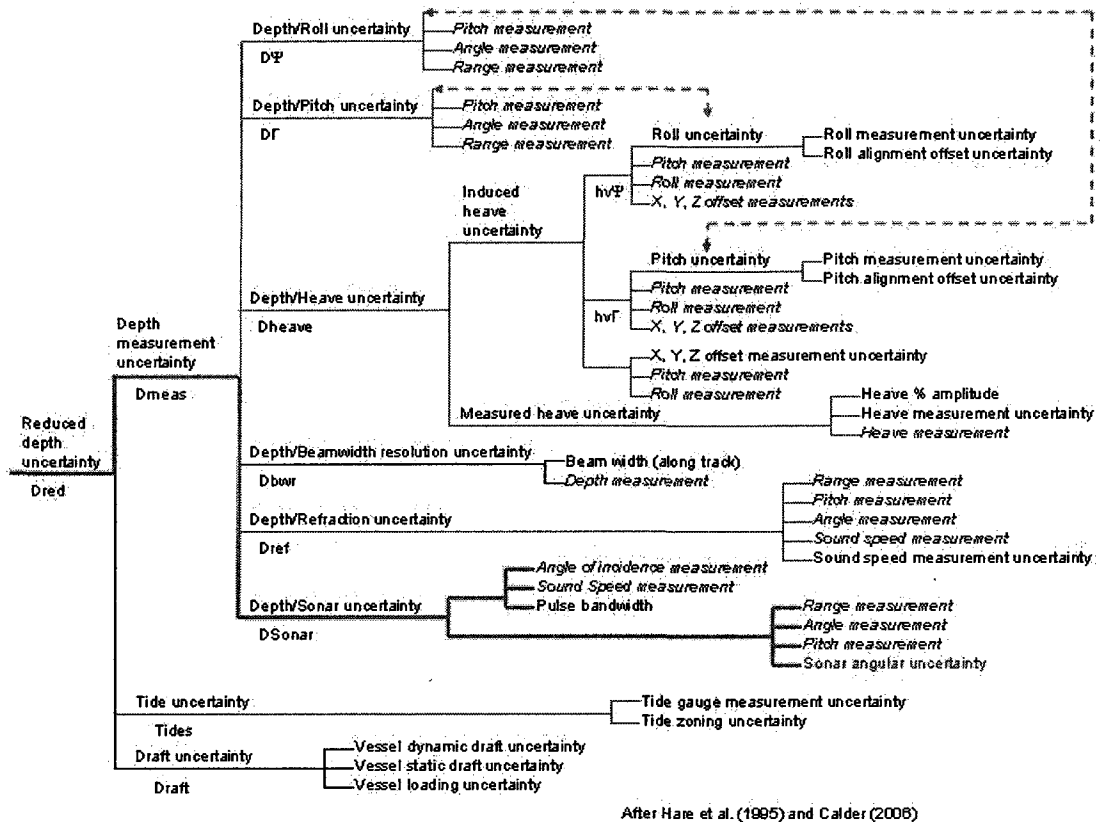


Figure 11: Uncertainty tree (After Hare, et al. (1995) and Calder (2006)). Uncertainties not being displayed include cross-terms for yaw uncertainty and heave, roll and pitch uncertainty on refraction, and heave uncertainty on refraction

The reduced depth uncertainty is the combination of the depth measurement uncertainty (σ_{Dmeas}), tide uncertainty (σ_{Tides}), and draft (σ_{Draft}).

These three uncertainty components are uncorrelated; therefore the reduced depth variance is shown below without covariance terms.

$$\sigma^2_{Dred} = \sigma^2_{Dmeas} + \sigma^2_{Tides} + \sigma^2_{Draft} \quad (62)$$

Although it could be argued that an uncertainty in the draft would affect some components of the depth measurement uncertainty (by having a direct impact on the depth of the sonar for ray tracing), it is assumed such a contribution would be extremely small for these data and will therefore be ignored.

The draft uncertainty is the combination of the uncertainty of dynamic draft (σ_{DynDraft}), static draft ($\sigma_{\text{StaticDraft}}$), and loading (σ_{Loading}). As described in section 2.2, each of the draft uncertainty components has a unique definition and consequentially they are considered uncorrelated. Although it is possible that by improperly modeling one draft component, the remaining components would be affected (i.e. not taking into account the change in static or dynamic draft due to significant loading condition changes), it is assumed that the draft components of the R/V Coastal Surveyor are well understood, measured, and modeled for the test data.

$$\sigma^2_{\text{Draft}} = \sigma^2_{\text{DynDraft}} + \sigma^2_{\text{StaticDraft}} + \sigma^2_{\text{Loading}} \quad (63)$$

The tide uncertainty is the combination of the tide gauge measurement uncertainty (σ_{TideMeas}) and the uncertainty associated with the tide zoning (σ_{TideZone}). The uncertainty of the tide gauge is wholly independent of the zoning component.

$$\sigma^2_{\text{Tides}} = \sigma^2_{\text{TideMeas}} + \sigma^2_{\text{TideZone}} \quad (64)$$

Depth measurement uncertainty is the combination of depth/pitch uncertainty ($\sigma_{\text{D}\Psi}$), depth/roll uncertainty ($\sigma_{\text{D}\Gamma}$), depth/heave uncertainty (σ_{Dheave}), depth/sonar uncertainty (σ_{Sonar}), depth/refraction uncertainty (σ_{Dref}), and covariance terms for heave, pitch and roll and refraction.

Starting with the covariance terms, the Roll term of induced heave is:

$$\left(\frac{\partial D_{\text{meas}}}{\partial D_{\text{hv}\Psi}} \right) = (X \cos(\Psi_{\text{att}}) \cos(\Gamma_{\text{att}}) - Z \sin(\Psi_{\text{att}}) \cos(\Gamma_{\text{att}})) \quad (65)$$

The Roll term of depth:

$$\left(\frac{\partial D_{meas}}{\partial D\Psi} \right) = (r_{est} \cos(\theta_{est}) \cos(\Gamma)) \quad (66)$$

Pitch from induced heave:

$$\left(\frac{\partial D_{meas}}{\partial Dhv\Gamma} \right) = (Y \cos(\Gamma_{att}) - X \sin(\Psi_{att}) \sin(\Gamma_{att}) - Z \cos(\Psi_{att}) \sin(\Gamma_{att})) \quad (67)$$

Pitch term of depth:

$$\left(\frac{\partial D_{meas}}{\partial D\Gamma} \right) = (r_{est} \cos(\theta_{est}) \sin(\Gamma)) \quad (68)$$

Pitch and roll from refraction:

$$\left(\frac{\partial D_{meas}}{\partial Dref\Gamma\Psi} \right) = \left(\frac{\cos(\theta_{est}) \cos(\Gamma)}{c_{est}} \right) \quad (69)$$

Heave from refraction:

$$\left(\frac{\partial D_{meas}}{\partial Dhv} \right) = \left(\frac{\sin(\theta_{est})}{c_{est}} \right) \quad (70)$$

To calculate the covariance terms for Pitch, Roll, depth and heave:

$$\sigma_{D\Gamma hv\Gamma} = \frac{1}{n} \sum_{i=1}^n (D\Gamma_i - \overline{D\Gamma})(hv\Gamma_i - \overline{hv\Gamma}) \quad (71)$$

$$\sigma_{D\Psi hv\Gamma} = \frac{1}{n} \sum_{i=1}^n (D\Psi_i - \overline{D\Psi})(hv\Psi_i - \overline{hv\Psi}) \quad (72)$$

To calculate the covariance terms for Pitch, Roll, heave, and refraction:

$$\sigma_{D\Gamma ref\Gamma\Psi} = \frac{1}{n} \sum_{i=1}^n (D\Gamma_i - \overline{D\Gamma})(ref\Gamma_i - \overline{ref\Gamma}) \quad (73)$$

$$\sigma_{D\Psi ref\Gamma\Psi} = \frac{1}{n} \sum_{i=1}^n (D\Psi_i - \overline{D\Psi})(ref\Psi_i - \overline{ref\Psi}) \quad (74)$$

$$\sigma_{Dhv refhv} = \frac{1}{n} \sum_{i=1}^n (Dhv_i - \overline{Dhv})(refhv_i - \overline{refhv}) \quad (75)$$

The covariance terms can be included in the measured depth uncertainty calculation, shown in equation (76). Although it is possible, under certain circumstances, that the covariance terms would be important for measured depth uncertainty, it is unlikely that the covariance terms would have a significant effect for this test data and will be ignored for calculation of the 5410 uncertainty model. Combining these terms with the individual uncertainty components results in the depth measurement uncertainty:

$$\sigma_{Dmeas}^2 = \left[\begin{array}{l} \sigma_{D\Psi}^2 + \sigma_{D\Gamma}^2 + \sigma_{Dheave}^2 + \sigma_{Dbw}^2 + \sigma_{Dsonar}^2 + \sigma_{Dref}^2 \\ + 2 \left(\begin{array}{l} \left(\frac{\partial Dmeas}{\partial D\Gamma} \right) \left(\frac{\partial Dmeas}{\partial hv\Gamma} \right) \sigma_{D\Gamma hv\Gamma} \\ + \left(\frac{\partial Dmeas}{\partial D\Psi} \right) \left(\frac{\partial Dmeas}{\partial hv\Psi} \right) \sigma_{D\Psi hv\Psi} \\ + \left(\frac{\partial Dmeas}{\partial D\Gamma} \right) \left(\frac{\partial Dmeas}{\partial ref\Gamma} \right) \sigma_{D\Gamma ref\Gamma\Psi} \\ + \left(\frac{\partial Dmeas}{\partial D\Psi} \right) \left(\frac{\partial Dmeas}{\partial ref\Psi} \right) \sigma_{D\Psi ref\Gamma\Psi} \\ + \left(\frac{\partial Dmeas}{\partial Dhv} \right) \left(\frac{\partial Dmeas}{\partial refhv} \right) \sigma_{Dhvrefhv} \end{array} \right) \end{array} \right] \quad (76)$$

Depth/Roll uncertainty is calculated from the estimated range, bearing and the roll uncertainty:

$$\sigma_{D\Psi}^2 = (r_{est} \sin(\theta_{est}) \cos(\Gamma))^2 \sigma_{\Psi}^2 \quad (77)$$

Depth/Pitch uncertainty is calculated from the estimated range, bearing and pitch uncertainty:

$$\sigma_{D\Gamma}^2 = (r_{est} \cos(\theta_{est}) \sin(\Gamma))^2 \sigma_{\Gamma}^2 \quad (78)$$

Depth/Heave uncertainty is the combination of the measured and induced heave.

$$\sigma^2_{Dheave} = \sigma^2_{InducedHeave} + \sigma^2_{MeasuredHeave} \quad (79)$$

Induced heave uncertainty is the combination of pitch, roll, offsets, pitch uncertainty, roll uncertainty, and offset measurement uncertainties.

$$\sigma^2_{inducedHeave} = \left[\begin{array}{l} (Y \cos(\Gamma_{att}) - X \sin(\Psi_{att}) \sin(\Gamma_{att}) - Z \cos(\Psi_{att}) \sin(\Gamma_{att}))^2 \sigma_{\Gamma}^2 + \\ (X \cos(\Psi_{att}) \cos(\Gamma_{att}) - Z \sin(\Psi_{att}) \cos(\Gamma_{att}))^2 \sigma_{\Psi}^2 + \\ (\sin(\Gamma_{att}))^2 \sigma_Y^2 + (\sin(\Psi_{att}) \cos(\Gamma_{att}))^2 \sigma_X^2 \\ +(1 - \cos(\Psi_{att}) \cos(\Gamma_{att}))^2 \sigma_Z^2 \end{array} \right] \quad (80)$$

Breaking up the heave uncertainty into different components, the heave and pitch components of heave can be used for covariance analysis.

$$\sigma^2_{InducedHeave} = \sigma^2_{hv\Psi} + \sigma^2_{hv\Gamma} + \sigma^2_{hvOff} \quad (81)$$

$$\sigma^2_{hv\Psi} = (X \cos(\Psi_{att}) \cos(\Gamma_{att}) - Z \sin(\Psi_{att}) \cos(\Gamma_{att}))^2 \sigma_{\Psi}^2 \quad (82)$$

$$\sigma^2_{hv\Gamma} = (Y \cos(\Gamma_{att}) - X \sin(\Psi_{att}) \sin(\Gamma_{att}) - Z \cos(\Psi_{att}) \sin(\Gamma_{att}))^2 \sigma_{\Gamma}^2 \quad (83)$$

$$\sigma^2_{hvOff} = (\sin(\Gamma_{att}))^2 \sigma_Y^2 + (\sin(\Psi_{att}) \cos(\Gamma_{att}))^2 \sigma_X^2 + (1 - \cos(\Psi_{att}) \cos(\Gamma_{att}))^2 \sigma_Z^2 \quad (84)$$

Pitch uncertainty is the combination of the sensor pitch measurement uncertainty and the uncertainty of the pitch bias estimate.

$$\sigma^2_{\Gamma} = \sigma^2_{\Gamma_{meas}} + \sigma^2_{\Gamma_{align}} \quad (85)$$

Roll uncertainty is the combination of the sensor roll measurement uncertainty and the uncertainty of the roll bias estimate.

$$\sigma^2_{\Psi} = \sigma^2_{\Psi_{meas}} + \sigma^2_{\Psi_{align}} \quad (86)$$

According to the manufacturer of the heave sensing unit, the heave uncertainty is the larger of either (a) a fixed component of heave or (b) a percentage of the measured heave.

$$\sigma^2_{MeasuredHeave} = \max(a^2, (bH_{meas})^2) \quad (87)$$

Depth/Beamwidth uncertainty is calculated from the fore-aft beamwidth (ϵ_Y) and depth below the sensor (z).

$$\sigma^2_{Dbw} = \left[z \left(1 - \cos\left(\frac{\epsilon_Y}{2}\right) \right) \right]^2 \quad (88)$$

Depth/Sonar uncertainty is the unknown and will be calculated from observed difference data in a later section.

$$\sigma_{Dsonar} = \langle UNKNOWN \rangle \quad (89)$$

Depth/Refraction uncertainty is calculated from the estimated range, bearing, pitch, estimated ray sound speed, and sound speed uncertainty.

$$\sigma^2_{Dref} = \left(\frac{r_{est} \cos(\theta_{est})}{c_{est}} \cos(\Gamma) \right)^2 \sigma_{cp}^2 + \left(\frac{r_{est} \sin(\theta_{est})}{c_{est}} \cos(\Gamma) \right)^2 \left[\left(\frac{\tan(\theta_{est})}{2} \right)^2 \sigma_{cp}^2 \right] \quad (90)$$

The total propagated uncertainties of all sources of uncertainty except those for the sonar can be calculated for individual soundings and for hypothetical scenarios. The total and individual uncertainties for all sources of uncertainty except the sonar are shown in Figure 12, assuming a scenario similar to that used during acquisition of the test data and a 20-m altitude.

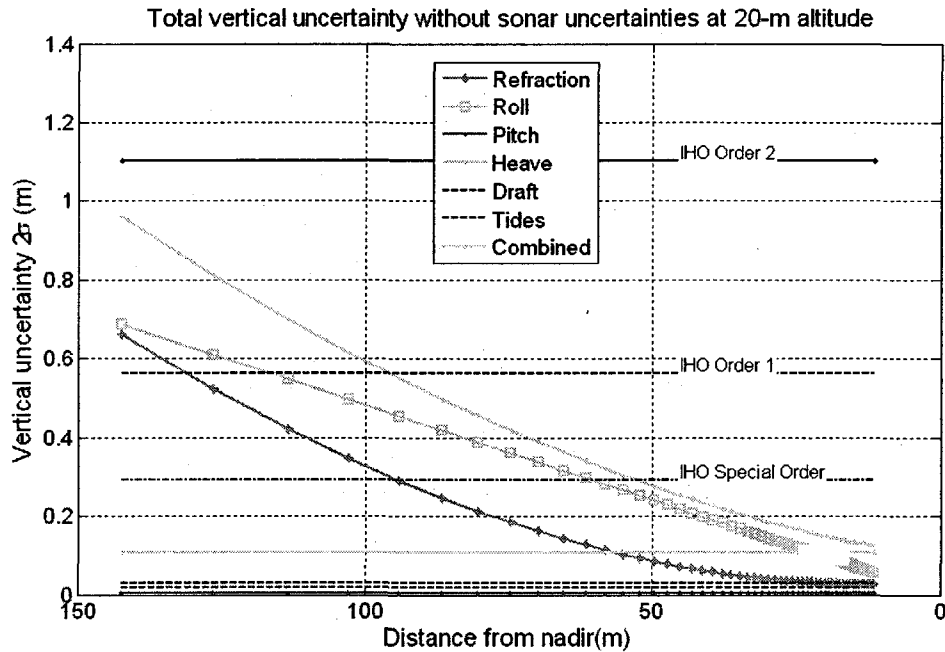


Figure 12: Total vertical uncertainty and individual uncertainties at 2σ without sonar uncertainties at 20-m altitude

3.2 Calculation of observed difference data

Once the uncertainties for all but the sonar are calculated, the next step needed to solve for the 5410 uncertainties is the calculation of difference data. Processed hydrographic data cleaning system (HDCS) data were exported from CARIS HIPS into a text format that was then imported into Matlab. Text files of surfaces created from 5410 PDS data and Kongsberg EM 3002 data were also exported from CARIS HIPS and imported into Matlab. Each surface was a regularly spaced grid, with equal Easting and Northing facets. Grid resolution is defined as the length of a full side of any given square cell (a one meter resolution grid cell has a length of one meter and a width of one meter). The grid node of a cell is the center of that cell. Each sounding position (Easting and Northing) was evaluated against grid node positions to find the nearest grid node

within a maximum horizontal radius (r_{Max}). The maximum radius term was used, consequently only grid cells in the vicinity of the sounding position were evaluated. In Figure 13, z_{Diff} is the vertical difference between the sounding ($z_{sounding}$) and the grid node depth (z_{grid}) and γ is the grid resolution. Grid cells were considered as horizontal entities. A negative value indicates that the sounding is shoaler than the grid node. A positive value indicates that the sounding is deeper than the grid node.

$$z_{Diff} = z_{caris} - z_{grid} \quad (91)$$

$$r_{Max} = \sqrt{2\gamma^2} \quad (92)$$

Although 5410 bathymetry data were manually edited in CARIS HIPS for gross errors for surface creation, all 5410 bathymetry were exported to Matlab and considered for analysis.

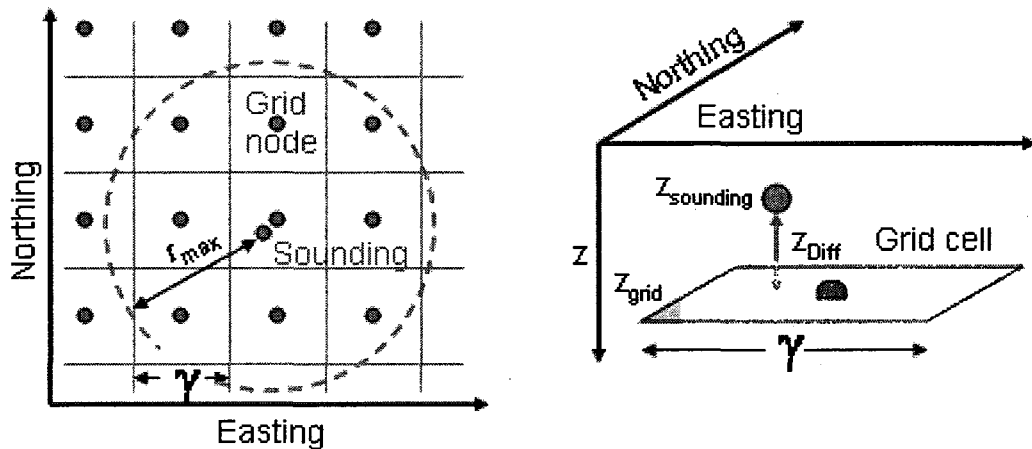


Figure 13: Determination of vertical difference between sounding and grid node using the grid resolution (γ) to determine the maximum search radius (r_{max}) for finding the nearest grid node for each sounding

3.3 Mean difference between 5410 soundings and reference surface

To determine if any systematic uncertainty was present in the difference data (z_{Diff}), the mean for any given angular sector (θ_a) can be calculated. Angular sectors are defined as all of the data with raw angle of arrival values within the bounds of the sector (i.e. 59.75° to 60.25°).

$$\overline{z_{Diff}(\theta_a)} = \frac{1}{n} \sum_{i=1}^n z_{Diff_i} \quad (93)$$

If no systematic uncertainty were present in the data, one would expect the mean of each angular sector to approach zero as more data are evaluated. This was not the case for the reviewed 5410 bathymetry. The mean for any given angular sector varied from line to line. As the results from multiple lines were summed, the mean of most sectors did not approach zero.

To perform uncertainty analysis using the difference data, it was necessary to remove the difference bias in the data so only random error was considered. The mean of each angular sector ($z_{filter}(\theta_a)$) for a given line was subtracted from the observed difference (z_{Diff}) to calculate the corrected observed difference ($z_{zeromean}$).

$$z_{zeromean}(\theta_a) = z_{Diff}(\theta_a) - z_{filter}(\theta_a) \quad (94)$$

A number of non-sonar sources of uncertainty that would be relatively constant for a single line would be extracted by removal of the mean. Tide and draft systematic errors would be extracted by removal of the mean. Any systematic bias from the sonar or sonar processing would also be extracted by removal of the mean. A modification to the processing code developed by Locke

reduced some of the mean bias for the port data, but not the starboard data.

Because port and starboard data show different biases, this suggests that the biases are at least partially sonar specific and not tide or draft induced.

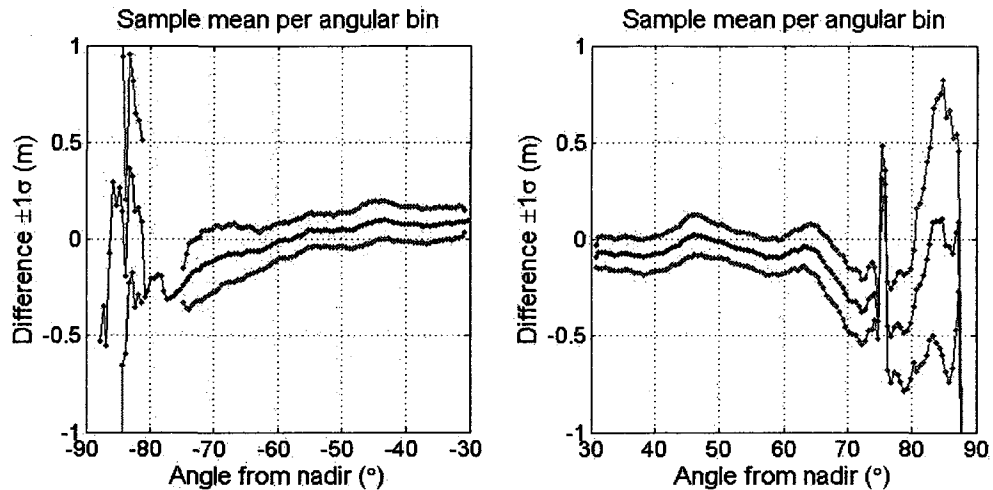


Figure 14: Sample mean (black dots) and standard deviation (blue pluses) for 51 lines binned in 0.5° sectors without filtering shows difference data irregularities. Port data is on the left and starboard data is on the right

Figure 14 may give the impression that all data showed the exact same filter results, but this was not the case. Each line had a slightly different angular bin means, with the general trends remaining (i.e. the inflection points at 45° and 65° in the starboard data were always visible, but the actual difference value varied). Figure 15 shows the results of the individual removed means used for each line. The data past 70° are not being shown since they were much more variable. The port side data, in general, had a higher trend (or peak) around 45°. The starboard data shows more defined peaks around 46° and 65°.

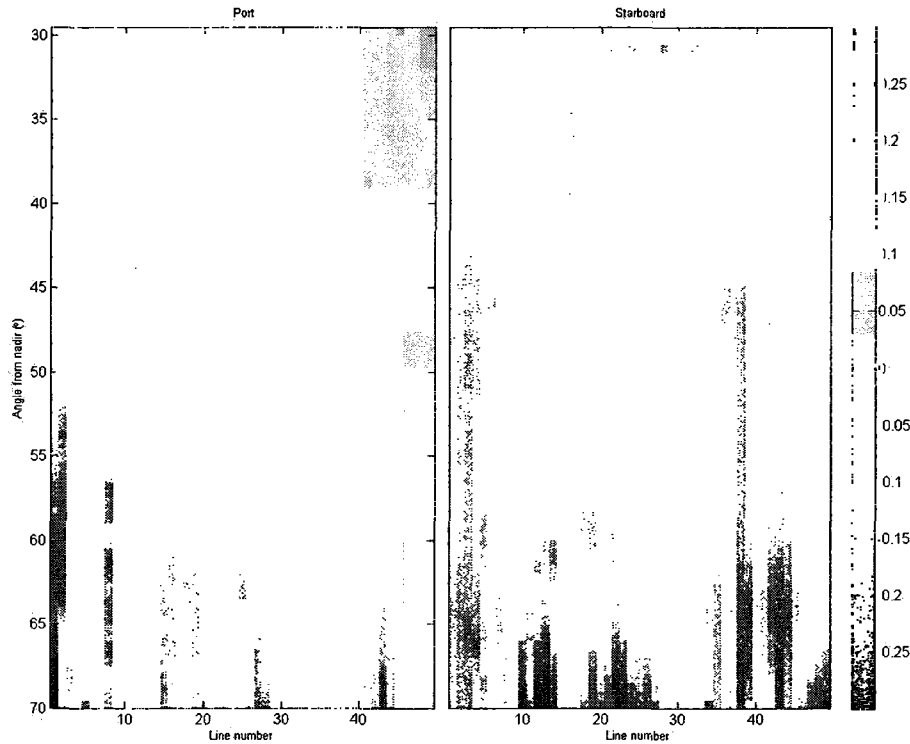


Figure 15: Mean filter results for individual lines. Horizontal axis is the line number and the vertical axis is angle from nadir. The color is based on the filter value in meters. Note that the starboard data on the right show peaks around 46° and 65°

Figure 16 shows the results of removing each line mean from each line. The data binned by angular sector for all of the lines now have a near zero mean. A discussion on the possible causes will follow later in this section but it should be noted again that a number of non-sonar errors could be removed by this filtering method. Those errors that in effect would create a static bias for the purposes of a single line are tides, draft, and sound speed profile. A distinction is made between uncertainty (as used in the rest of this document) and error here because at this point an estimate exists of the difference between the true and measured values. The systematic error (or bias) is removed from the data in

order to analyze the random uncertainties of the data. If the difference data were not de-trended then the assumption that the sonar uncertainties are random cannot be made when solving for those uncertainties.

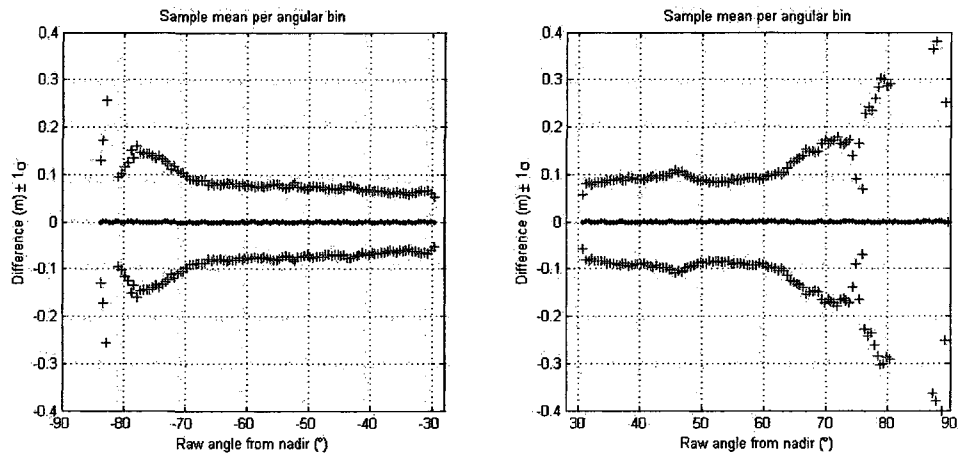


Figure 16: Sample mean (black dots) and standard deviation (blue pluses) for 51 lines binned in 0.5° sectors with filtering. Port data on the left and starboard data on the right

The difference data can be categorized by bottom type shown in Figure 17. Using an existing bottom type map by Ward [48], all individual points for a given angular bin can be separately evaluated by bottom category. Figure 17 shows histogram for three different bottom types for a single angular sector. Although the histograms do vary slightly from each other (slightly different variances), the differences may be more the result of sample size rather than showing different performance based on bottom type. Angular uncertainty results will be evaluated against bottom type in a later section.

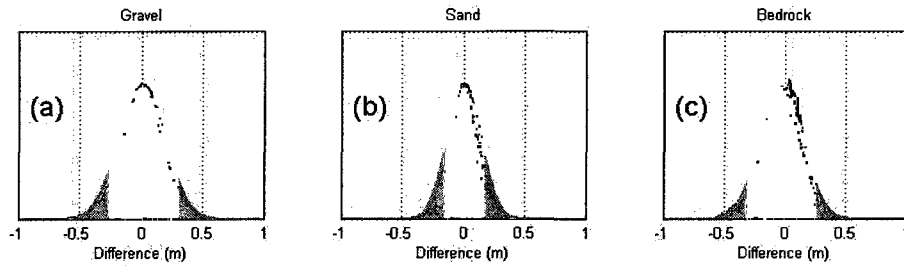


Figure 17: Histograms of de-trended difference data for a single angular bin for 51 lines for gravel (a), sand (b), and bedrock (c) where the red line is the Gaussian fit.

There are two hypotheses for the cause of the apparent bias removed by filtering each line: (1) a meandering DC basis for each element and (2) multipath interference.

In work by Glynn [14], it was assumed that the DC bias of any receive element was static and did not change for a given set of data. In that work, the static DC bias was removed in processing. The first hypothesis, which has been proposed by de Moustier (de Mousiter, 2008, Personal Communication), is that the DC bias for each channel was not static but changed over time. A non-static DC bias would have a detrimental effect on the phase difference (and therefore angle of arrival estimation) solution and would increase the uncertainty. It is also true, but harder to show, that a drifting DC bias could create a constant bias in the difference data.

The second hypothesis is that the difference bias is the result of multipath interference. Using the technique for determining phase errors due to interference described by Denbigh [16], the mean and standard deviation anomalies could be explained by back calculating the most likely source of noise interference. The probability density function of the phase error can be expressed as:

$$p(\varphi) = \frac{J^2}{2\pi\sigma^4} \left[\frac{1}{1-A^2} - \frac{A}{(1-A^2)^{3/2}} \left\{ \frac{\pi}{2} - \sin^{-1} A \right\} \right] \quad (95)$$

Using the simplified assumption derived by Denbigh [16] where P_s is the signal power, P_I is the noise power, φ_s is the signal phase, and φ_I is the noise phase.

$$\sigma^2 = P_s + P_I \quad (96)$$

$$\rho = P_s \cos \varphi_s + P_I \cos \varphi_I \quad (97)$$

$$\eta = -(P_s \sin \varphi_s + P_I \sin \varphi_I) \quad (98)$$

$$A = (\eta \sin \varphi - \rho \cos \varphi) / \sigma^2 \quad (99)$$

$$J^2 = \sigma^4 - \rho^2 - \eta^2 \quad (100)$$

Assuming that the two way travel time for the interference must match that of the signal, and that the most likely causes of interference are those paths with the minimum number of surface or bottom bounces, each given angle of arrival has one or two possible noise sources.

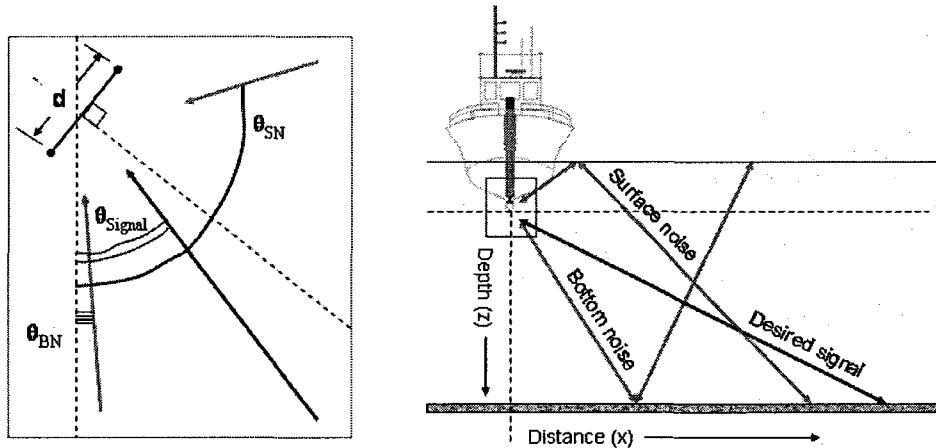


Figure 18: Multipath noise sources: desired signal path (black line), interference paths (red lines). Inset: pair of receivers separated by distance (d)

Each multipath ray is a sum of two separate rays. Using the zero gradient assumption, each ray leg can be considered a single ray with a single angle of arrival. Due to the zero gradient assumption, the range traveled by the signal ray (s_{Signal}) will be the same as the two sources of interference (s_{BN} and s_{SN}).

$$\theta_{\text{SN}} = \cos^{-1} \left[- \left(\frac{(z + 2z_{\text{Sensor}})}{s_{\text{Signal}}} \right) \right] \quad (101)$$

$$\theta_{\text{BN}} = \cos^{-1} \left[\frac{(2z + z_{\text{Sensor}})}{s_{\text{Signal}}} \right] \quad (102)$$

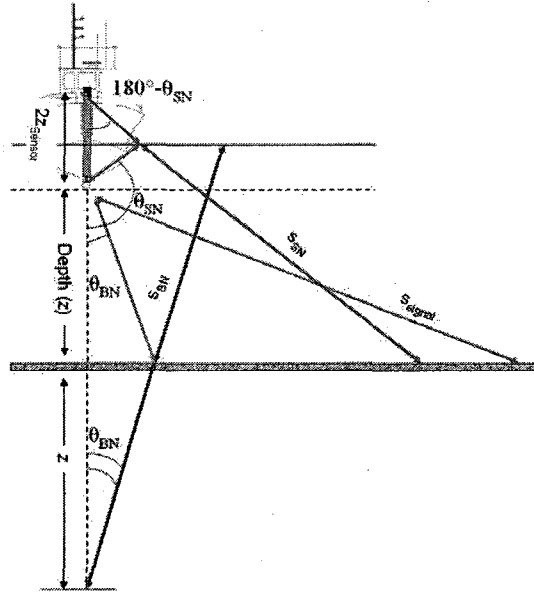


Figure 19: Bottom and surface multipath angle calculation showing surface and bottom angles. Bottom noise distance (s_{BN}) and surface noise distance (s_{SN}) equals signal path distance (s_{Signal}). Bottom noise angle (θ_{BN}) and signal noise angle (θ_{SN}) is a function of sensor depth (z_{Sensor}), depth (z) and signal distance.

The resultant noise source locations are shown in Figure 20 with the original signal source direction. Bottom and surface multiples could have a significant effect on the mean and standard deviation of the phase difference solution. The actual geometry for any given ping changes over time (as the

sonar is deeper or shallower in the water column and as the vessel moves), but there is an average sonar depth, roll, and pitch which would be reflected in the phase difference error results.

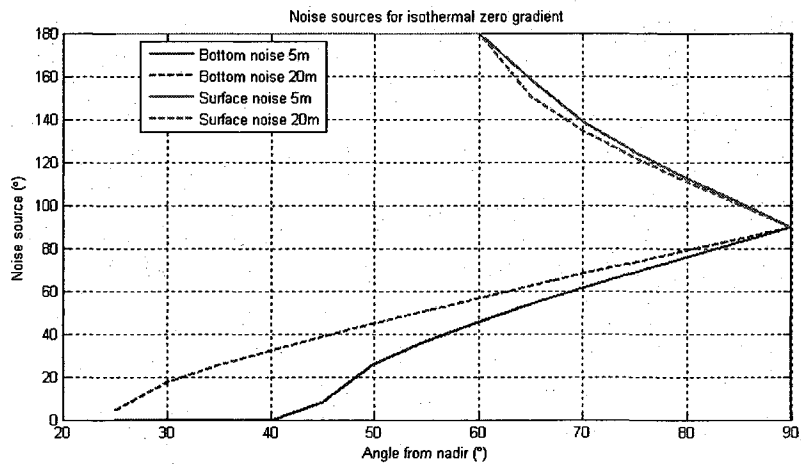


Figure 20: Noise source vs signal source for 5-m and 20-m depths assuming a sensor depth of one meter and zero sound speed gradient

3.4 Effect of signal-to-noise ratio (SNR)

As the SNR decreases (signal power usually decreases with range and relative noise power increases), the bias (difference between the expected solution and the mean of the calculated phase difference solution) increases.

The variance of the phase difference solution also increases as the SNR decreases. SNR (dB) is calculated from the noise and signal power:

$$SNR = 10 \log_{10} \left(\frac{P_s}{P_I} \right) \tag{103}$$

Using a single pair of elements as an example, the mean of a phase solution moves away from zero and the variance increases as the signal to noise ratio decreases. A bias in the phase solution would result in a bias of the angle of arrival solution and would therefore create a bias in the difference data. An

example probability density function of the phase error is shown for a single element pair with different signal to noise values in Figure 21. At lower signal to noise values the phase error ceases to be centered on zero.

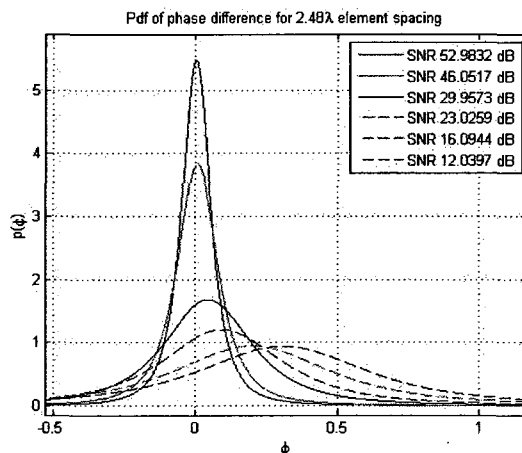


Figure 21: Probability density function (pdf) of phase difference error from equation (95) for source at bore sight, (70°), noise from surface reflection (117°) at different SNR from equation (103). Decreases in SNR result in the mean of the pdf shifting towards the noise solution and increasing standard deviation

Comparing three different element distances shown in Figure 22, the phase bias can be different for each element pair.

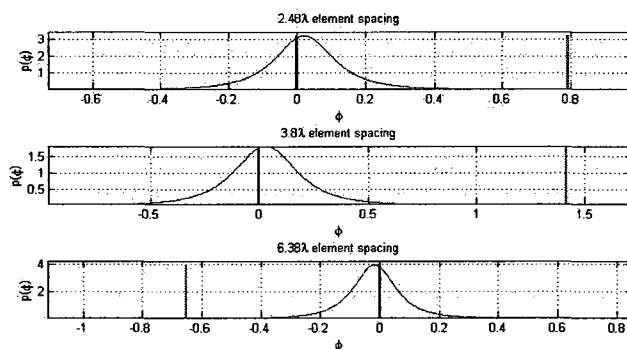


Figure 22: Probability density functions of phase error for three different element spacing from equation (95) where the source is at boresight (70°), phase for each pair shown with the black line, and noise from surface reflection (117°), phase for each pair shown with the red line

Although the Denbigh equations do offer an explanation for the resulting difference data irregularity, the more probable explanation is the non-stationary of the DC bias. It is highly unlikely that multipath interference for any given angular region would be consistent enough over time to cause an angular bias for that angular region. Much more likely is that multipath interference will over time cause the angular uncertainty for a given angular sector to increase.

3.5 Time resolution (pulse bandwidth)

The sonar depth uncertainty from the pulse bandwidth is the first component to be discussed for the 5410. Pulse bandwidth impacts the range uncertainty, which in turn affects the sonar vertical uncertainty. Vertical measurement uncertainty due to pulse bandwidth ($\sigma^2_{\text{SonarBW}}$) can be approximated with the angle of incidence (θ_{Inc}), speed of sound (c), range sampling distance (Δr_s), and the pulse duration (τ) in seconds. Hare et al. [29, 30] used the equation below from Hammerstad [49]:

$$\sigma^2 \text{Sonar}_{\text{BW}} = \cos^2 \theta_{\text{Inc}} \left(\left[\frac{\Delta r_s}{2} \right]^2 + \left[\frac{c\tau}{4} \right]^2 \right) \quad (104)$$

The angle of incidence is being used rather than the bearing and pitch because the angle of incidence of a given ray on the seafloor will affect the depth uncertainty from the pulse bandwidth. Figure 23 shows a diagram of the effect of pulse bandwidth on the area of the seafloor ensonified.

This means that there are $\left(\frac{\Delta R_{BW}}{\Delta R_t} \cong 4.7\right)$ range samples for each range

resolution cell. Assuming a uniform distribution of the samples within each resolution cell whose end points are defined as:

$$(\Delta R_{iN} - \Delta R_{i0}) = \left(\frac{\Delta R_{BW}}{\Delta R_t}\right) \Delta R_t \quad (107)$$

the variance of these samples is:

$$\sigma_x^2 = \frac{(\Delta R_{iN} - \Delta R_{i0})^2}{12} \quad (108)$$

Therefore,

$$\sigma^2_{Sonar_{BW}} = \left(\frac{c}{2BW}\right)^2 / 12 = \left(\frac{c}{BW}\right)^2 / 48 \cong \left(\frac{c}{7BW}\right)^2 \quad (109)$$

A detrimental aspect of the GSF format currently used for the 5410 data is the time resolution for two way travel time in the test data. From the sampling frequency (f_s), one would expect a minimum time resolution of 4.4×10^{-5} s, but the GSF data analyzed only supported 10^{-4} s. Although the GSF format does support scale factors [50], they were not utilized in the right way for the test data. It is recommended that for future analysis, the optional scale factor field be utilized correctly for 5410 GSF data to allow increased time resolution. Whenever the sampling rate of the sonar (Δt_{Sonar}) is smaller than the GSF time resolution (Δt_{GSF}), the discrepancy introduces a range resolution uncertainty independent of the sonar shown as:

$$\Delta R_{GSF} = \left[\frac{c \left(\Delta t_{GSF} - \left[\frac{1}{f_s} \right] \right)}{2} \right] / 2 \quad (110)$$

Combining these two components results in the depth uncertainty due to bandwidth and time resolution:

$$\sigma^2 \text{Sonar}_{BW} = \cos^2 \theta_{inc} \left(\left(\frac{c}{7BW} \right)^2 + \left[\left(\frac{c}{4} \right) \left(\Delta t_{GSF} - \left[\frac{1}{f_s} \right] \right) \right]^2 \right) \quad (111)$$

If future 5410 GSF format data utilize the two way travel time scale factor, then the second term can be eliminated from future versions of 5410 uncertainty models.

3.6 5410 Signal Processing

The description of the 5410 processing method used by Glynn [14] is important in understanding the results of the angular uncertainty that will be presented in chapter 4. Since the 5410 data are processed using a method that differs from other phase differencing systems, it is reasonable to assume that the angular uncertainty will also be different than predicted from those other methods.

Glynn [14] describes the equations using phasor processing techniques to solve the differential phase measurements between multiple receivers. The same equations can be used to solve for the magnitude from multiple receivers. This is the method used by Locke (Locke, 2008, Personal Communication) after filtering the real and imaginary components.

Glynn [14] filters the real and imaginary components using an FIR filter. The differential phase solution for each bathymetric pair are filtered using a variable length FIR filter that used an increasing number of samples farther out in the swath after 45°. After filtering, the three phase difference solutions are used to calculate the angle of arrival. Vector averaging of the three solutions is used, with an angular tolerance, so outlier angle of arrival estimates from a single pair do not unduly weight the final solution. The reported angle of arrival from the processing method should be described as the estimated angle of arrival since it is the product of multiple filtering steps and vector averaging. The practical effects of filtering mean that the resulting bathymetry can be much less noisy than data not processed using this method.

Lurton has proposed a number of equations describing the angular uncertainty for a system based on the signal to noise ratio [11, 12]. These equations were not used due to the differences in processing methods implied in the Lurton articles and those used for test 5410 data [14]. Lurton also shows a similar equation utilizing the signal to noise ratio and other data for the sonar depth uncertainty [30]. These equations were not used for this analysis.

3.7 Angular Uncertainty

The angular uncertainty is the second component of the sonar depth uncertainty. Angular uncertainty can be approximated using the de-trended vertical difference data (z_{zeromean}). Assuming that any angular uncertainty would vary for each side and angular sector from nadir, the difference data from

multiple lines can be evaluated. Figure 24 shows a histogram of de-trended depth difference data for a 0.5° bin from multiple lines.

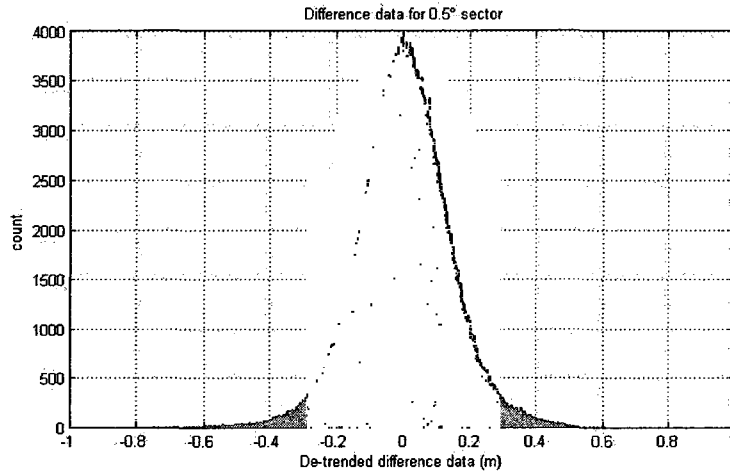


Figure 24: Histogram of depth difference data for single angular sector (69.75° to 70.25°)

The difference between the estimated (θ_{est}) and observed angles is the approximation of the angular error. The sample estimate of variance of the angular error is the angular uncertainty. The observed angle could be approximated by using the measured depth (z), depth difference ($z_{zeromean}$), and pitch (Γ).

$$\theta_{Observed} = \cos^{-1} \left[\frac{\cos \left[\cos^{-1} \left(\frac{z - z_{zeromean}}{r_{est}} \right) \right]}{\cos(\Gamma)} \right] = \cos^{-1} \left[\left[\frac{(z - z_{zeromean})}{r_{est}} \right] \right] \quad (112)$$

Taking the difference between the estimated and observed angle gives the estimated angular error. The weakness with using this method to calculate the angular uncertainty for the sonar is that all sources of uncertainty are being considered as angular uncertainty. This problem is overcome in equation (114) as all of the depth uncertainties are considered before solving for the angular

uncertainty. Figure 25 shows a histogram of angular error from the de-trended depth difference data from Figure 24.

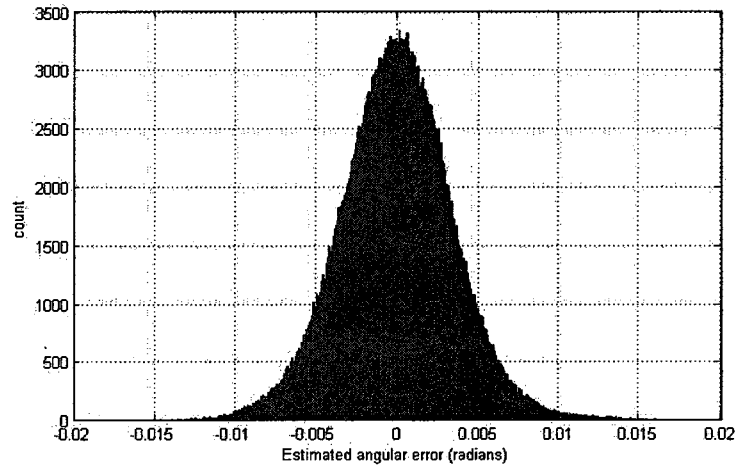


Figure 25: Histogram of estimated angular error for single angular sector (69.75° to 70.25°)

The variance of the distribution shown in Figure 25 would be the estimated angular uncertainty for this angular sector. Solving for all angular sectors, an approximate angular uncertainty model was generated, which is presented in Figure 26.

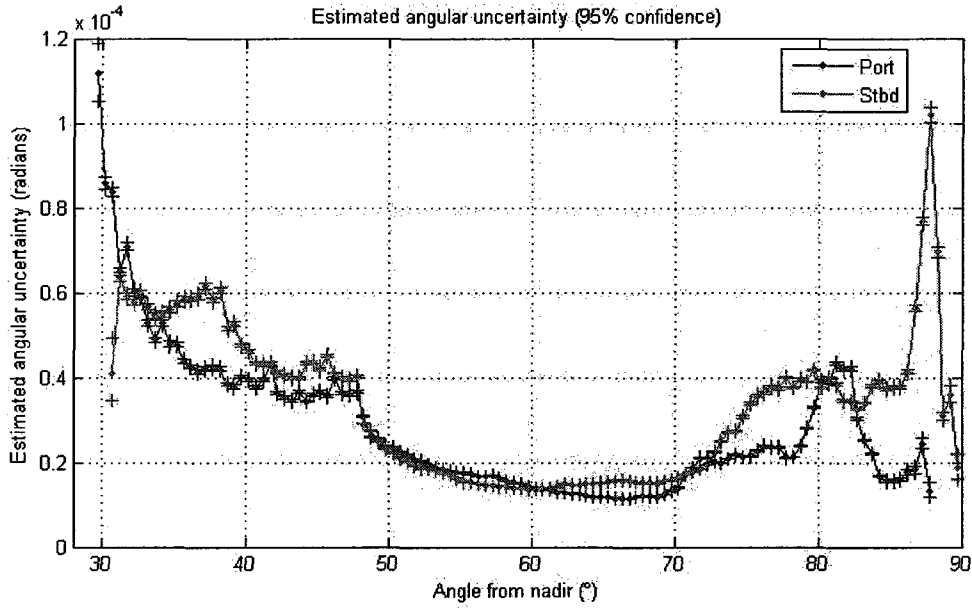


Figure 26: Estimated angular uncertainty assuming all observed uncertainties are the result of the sonar angular uncertainty

Since this model represents the cumulative effects of all sources of uncertainty, it cannot be used as a model solely for the angular uncertainty of the 5410. A more appropriate approach is to consider the angular uncertainty as part of a larger set of equations describing the total uncertainty.

As derived by Hare, et al. [29], the portion of the sonar uncertainty related to the angle solution can be calculated using the estimated range (r_{est}), estimated angle (θ_{est}), pitch (Γ), and the sonar angular uncertainty ($\sigma^2\theta_{Sonar}$). If all of the other uncertainties are known and the observed data uncertainty is known, then the sonar angular uncertainty can be solved.

$$\sigma^2 Sonar_{\theta} = (r_{est} \sin \theta_{est} \cos \Gamma)^2 \sigma^2 \theta_{Sonar} \quad (113)$$

Equations (111) and (113) can be combined for the sonar depth uncertainty shown in equation (114).

$$\sigma^2_{DSounder} = \left[\begin{array}{l} \cos^2 \theta_{inc} \left(\left(\frac{c}{7BW} \right)^2 + \left[\left(\frac{c}{4} \right) \left(\Delta t_{GSF} - \left[\frac{1}{f_s} \right] \right) \right]^2 \right) \\ + (s(\sin \theta_{est}) \cos \Gamma)^2 \sigma^2_{Sonar} \end{array} \right] \quad (114)$$

It is incorrect to assume that the standard deviation of the difference data from each angular sector can be used to solve for the angular uncertainty. Since each bin of de-trended difference data represent a variety of measured depths, ranges, and angles of incidence, all line data were evaluated against the calculated uncertainties to determine what value for angular uncertainty would account for 95% or more of the absolute value of the difference data. The cross terms (covariance) were not used in the calculations. Equation (115) was used to solve for the angular uncertainty.

$$0.95 = \frac{1}{n} \sum_{i=1}^n \left\{ \left| z_{zeromean} \right| \leq 1.96 \left[\begin{array}{l} \sigma^2_{DHeave} + \sigma^2_{D\Gamma} + \sigma^2_{D\Psi} + \sigma^2_{Dbw} + \sigma^2_{Sonar_{BW}} \\ + \sigma^2_{Tides} + \sigma^2_{Draft} + \\ (r_{est} \sin \theta_{est} \cos \Gamma)^2 (\sigma^2_{Sonar}) \end{array} \right]^{1/2} \right\} \quad (115)$$

CHAPTER 4

RESULTS

With the uncertainty values and difference data calculated in chapter 3, the 5410 angular uncertainty can be modeled. The 5410 angular uncertainty ($\sigma^2_{\theta_{\text{Sonar}}}$) was separately determined for each side of the sonar. Data were divided into short segments along a single track of echosounding and designated as a line. Each line represented approximately one minute of data and was categorized by the amount of observed acoustic backscatter imagery artifacts caused by multipath. Imagery artifacts coincided with strongly defined thermocline in the sound speed profiles and are considered separately since the resulting data represent the effect of the environment on the 5410 rather than the performance of the 5410 when evaluated alone. See Appendix D for information on sound speed, salinity, and temperature profiles acquired for this test.

It should also be noted that the performance of the port and starboard sides differed significantly. Although this difference is carried through in later analysis, it is reasonable to expect that any future 5410 PDS systems will have consistent performance for both the port and starboard sides. Glynn [14] proposed that observed differences in transducer performance could be the result of variations in manufacturing methods used when the transducers were built.

Angular uncertainty values were stratified by bottom type by determining whether each sounding resided in specific polygon bottom type regions created from a modified bottom type map from Ward [48]. There were some differences between the gravel and sand data, with greater differences between these two and bedrock data. Figure 27 shows the calculated angular uncertainty for the three bottom types. It is apparent that the angular uncertainty increased rapidly at 70° for both port and starboard gravel data when compared to sand data. Also apparent is the greater angular uncertainty for bedrock areas.

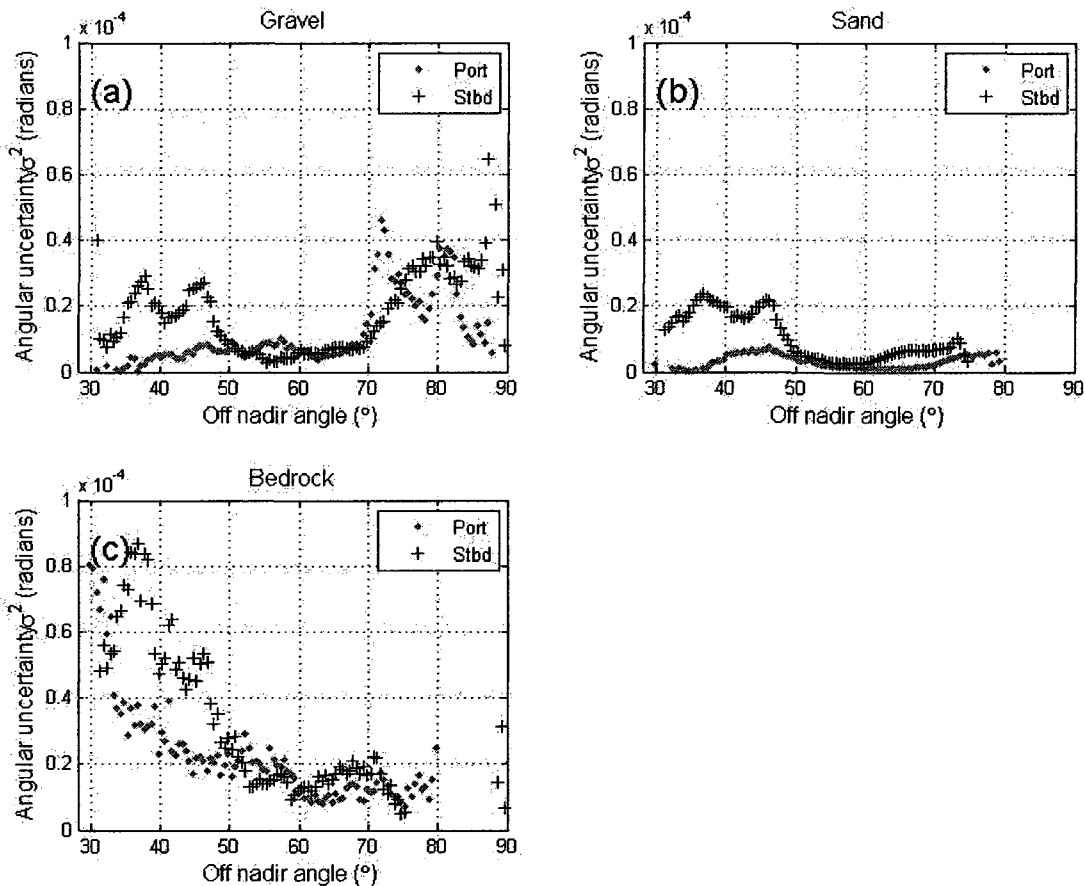


Figure 27: Calculated angular uncertainty for gravel (a), sand (b), and bedrock (c), for data without multipath negative sound speed gradient artifacts

The poor results from the bedrock data have two possible explanations. The first explanation is that the sonar performed poorly over areas where the bottom was complex with respect to the resolution of the reference surface resolution (one meter). The second explanation is that the 5410 was recording the depths of underwater vegetation growing on the bedrock. No direct observations were made to determine whether vegetation was growing on the bedrock at the time of the experiment. Additional work outside the scope of this analysis is necessary to resolve this problem.

If the impact of multipath artifacts due to negative sound speed gradient is extrapolated to 5410 bathymetry from acoustic backscatter imagery, it would be expected that the calculated angular uncertainty out to a coincident angle from nadir would match that from data without artifacts. Figure 28 shows the angular uncertainty calculated from lines with artifacts classified by bottom type for sand and gravel. The results for sand roughly match that shown in Figure 27 except that the angular uncertainty rapidly increases at 70°. The gravel angular uncertainty for data with artifacts is less well defined but also increases at 70° suggesting that multipath effects after 60° are being observed.

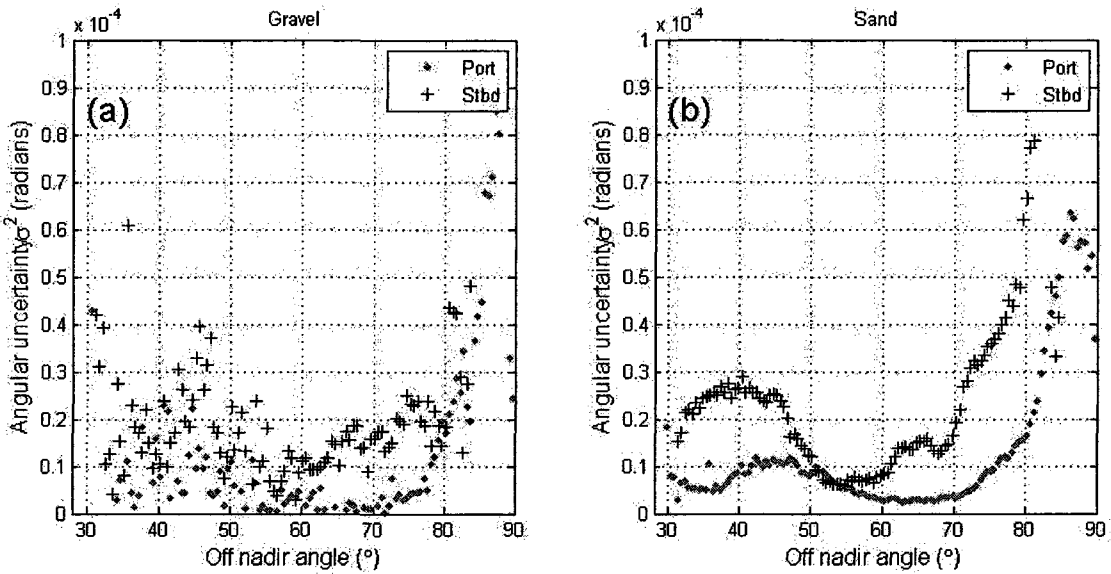


Figure 28: Calculated angular uncertainty for negative gradient multipath for gravel (a) and sand (b)

Angular uncertainty can also be evaluated against the angle of incidence calculated in Chapter 2. If the 5410 bathymetry has an angular dependence similar to that of the acoustic backscatter it would be expected to be apparent in the angular uncertainty results shown in Figure 29. The angular uncertainty results represented here do differ from those shown in Figure 27 but do not necessarily show distinct incidence angle dependence. The prominent spike in angular uncertainty for gravel in Figure 27 has become more gradual and less abrupt in Figure 29. Based on these results it cannot be demonstrated that there is a reduction in bathymetric performance due to a critical angle of incidence.

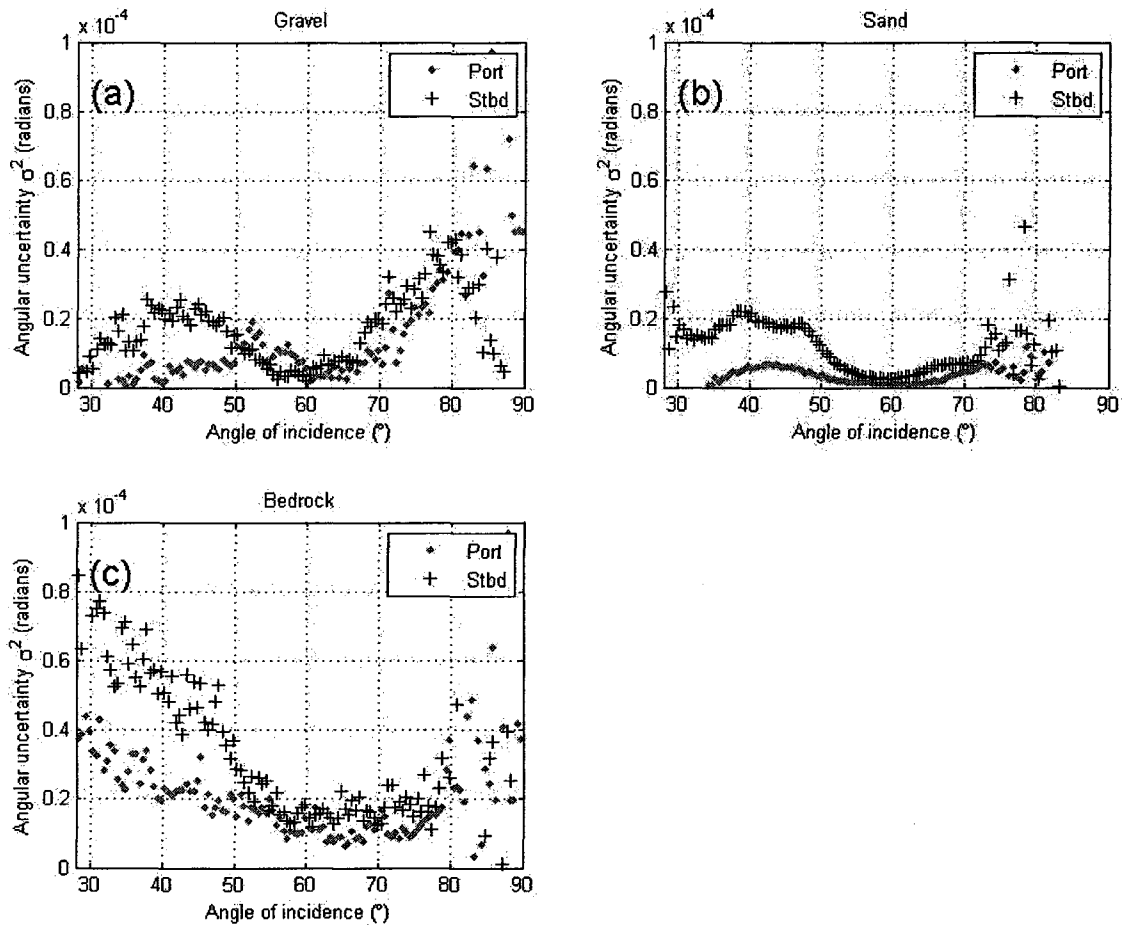


Figure 29: Calculated angular uncertainty for gravel (a), sand (b), and bedrock (c) by angle of incidence on the seafloor

Based on the unresolved issues associated with results in gravel and rock areas, the angular uncertainty results from the sand data were used. Portions of the sand data with no angular uncertainty results were extrapolated near nadir and the outer swath to produce an angular uncertainty model for the 5410. The sand data did not have angular uncertainty results out to 90° due to the bottom geometry of the sand test data and range scale used when compared to the other areas. This model shown in Figure 30 will be used to evaluate potential sonar performance in the next chapter.

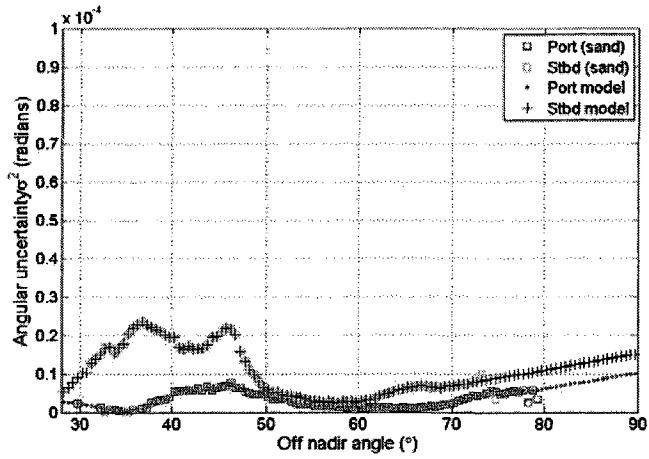


Figure 30: Extrapolated angular uncertainty model based on data acquired over sand showing the original data (squares) along with the model data (points and pluses)

The total propagated uncertainties from the CARIS HIPS export, calculated angular uncertainty and the observed uncertainties are plotted in Figure 31. In general, the exported CARIS HIPS uncertainty values underestimated the total uncertainty. The starboard angular uncertainty model shows up in the figure as a distinct peak around 43°.

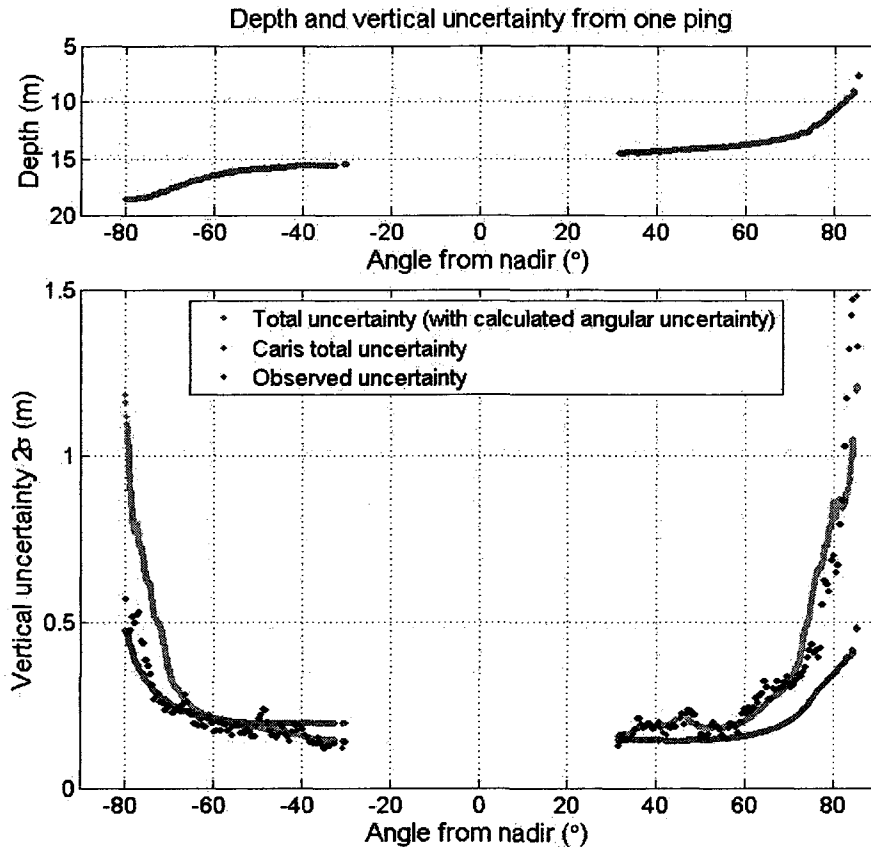


Figure 31: Top figure showing surface depth for single ping. Bottom figure showing total vertical uncertainties at 2σ for single ping showing exported CARIS HIPS, and calculated angular uncertainty model results with observed uncertainty

Although the exact uncertainty equations utilized by CARIS HIPS are not known, the differences between the total uncertainty using equation (63) and that exported from CARIS HIPS are most likely caused by different uncertainty equations for pulse bandwidth, and angular uncertainty (equation (115)). The results for the 5410 angular uncertainty computed in this analysis are considered more reflective of actual uncertainty as justified by the analysis.

CHAPTER 5

EVALUATION OF UNCERTAINTY MODEL WITH OCEAN MAPPING STANDARDS

Assuming a basic survey scenario similar to that carried out during acquisition of the test data, the angular uncertainties derived from the sand data combined with all other sources of uncertainty were used to predict performance for two different sonar altitude values (5 m and 20 m) representing the normal range of many NOAA hydrographic surveys, with the results presented in Figure 32.

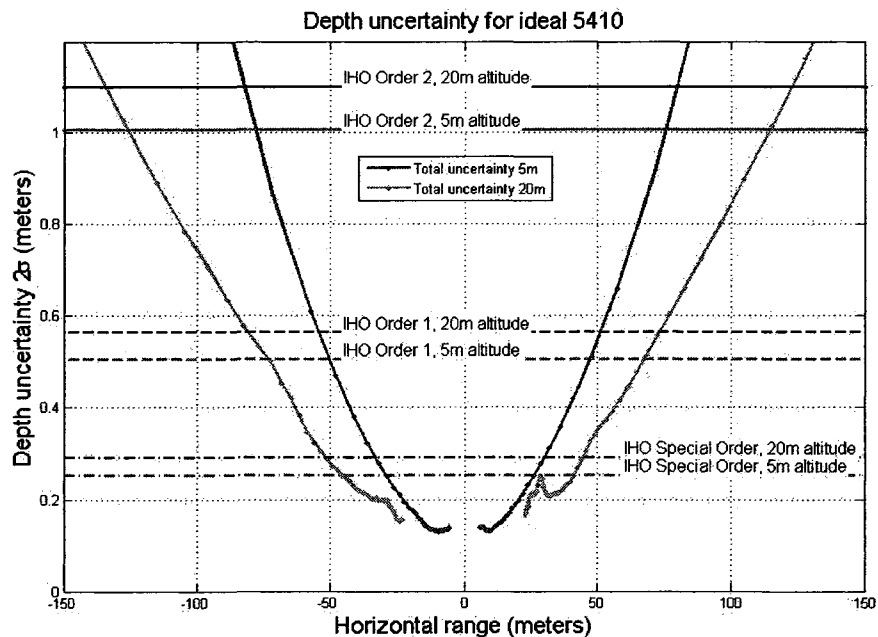


Figure 32: Theoretical total vertical uncertainty for ideal 5410 for altitudes of 5-m and 20-m showing null at nadir and IHO standards for each depth

The International Hydrographic Organization (IHO) promulgates uncertainty standards for hydrographic surveys by dividing these standards into categories or “Orders” appropriate for different navigational situations. Special Order is the most stringent, Order 1 is most broadly applicable, and Order 2 applies to less critical areas. Based on Figure 32, one could expect to acquire data meeting the IHO Special Order criteria out to 38 m from nadir, Order 1 out to 50 m, and Order 2 out to 75 m for a sonar altitude of five meters. Increasing the altitude to 20-m, but keeping all the basic assumptions the same, one could expect to acquire data meeting IHO Special Order criteria out to 50 m, Order 1 out to 80 m, and Order 2 out to 125 m under the same survey scenario as that carried out during the test data acquisition.

It may be useful to consider performance in a variety of less than ideal circumstances. Figure 33 shows the theoretical performance of the 5410 if the DC bias is not resolved. The variance and mean results shown in Figure 14 has been re-introduced into equation (63) and the absolute value of the mean added to the total propagated uncertainty. The performance for both depth ranges appreciably degrades with only a portion of the swath meeting IHO Order 2 for both depth ranges.

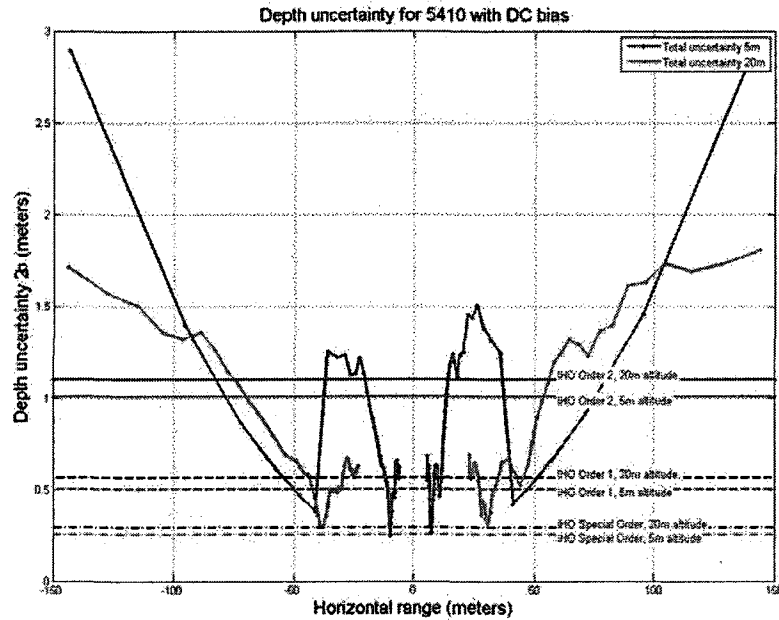
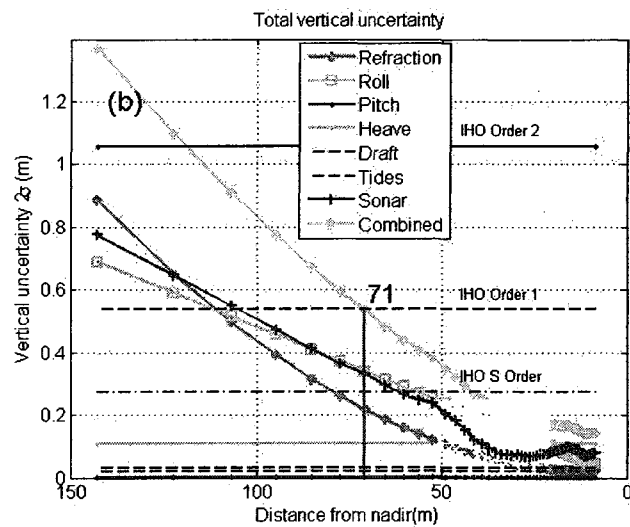
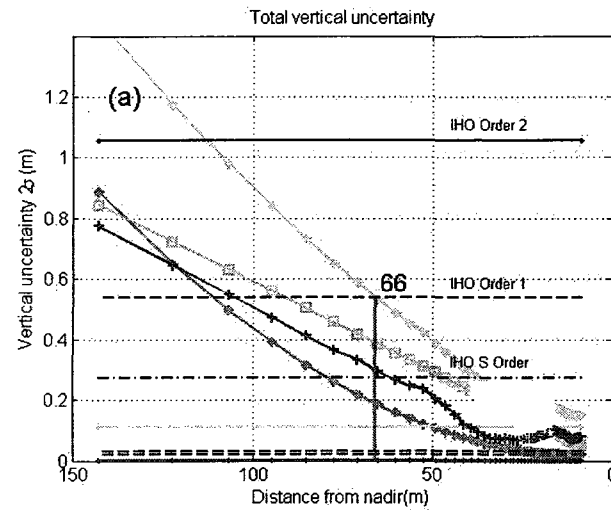


Figure 33: Theoretical vertical uncertainty for a 5410 with a DC bias. Neither depth range meets IHO Special Order, and only a portion of the swath meets IHO Order 2.

The swath covered by usable bathymetry is usually less than that covered by usable acoustic backscatter imagery in the test data. In other words, at a 75-m range scale, the 5410 acoustic backscatter imagery reaches out to 75 m, but the bathymetry may only reach out to 65 m to 70 m.

Figure 34 shows three scenarios for total vertical uncertainty for the 5410 for an altitude of 15-m. All sources of uncertainty are the same with the exception of changes to the roll, pitch, heave, and refraction uncertainties. Figure 34 (a) shows the results from using the same attitude sensor as used for the experiment with the only difference that DGPS correctors rather than RTK is being used. The use of DGPS correctors for this attitude sensor increases the uncertainty for roll and pitch (0.020°). Figure 34(b) shows the results for exactly the same scenario as used for the test. Figure 34 (c) shows the results by using an improved attitude sensor and improved sound speed uncertainty. The

improved attitude sensor reduces the uncertainties associated with roll, pitch, and heave (roll/pitch uncertainty 0.005° , heave 0.035 m and heave as 3.5% of amplitude). The uncertainties associated with sound speed were also reduced to 0.5 m/s. Figure 34 (a) has the smallest expected swath width out to IHO Order 1 reaching 8.7 times the water depth. Figure 34 (b) is expected to reach 9.5 times water depth and Figure 34 (c) is expected to reach 11 times the water depth. All three scenarios have no data at nadir.



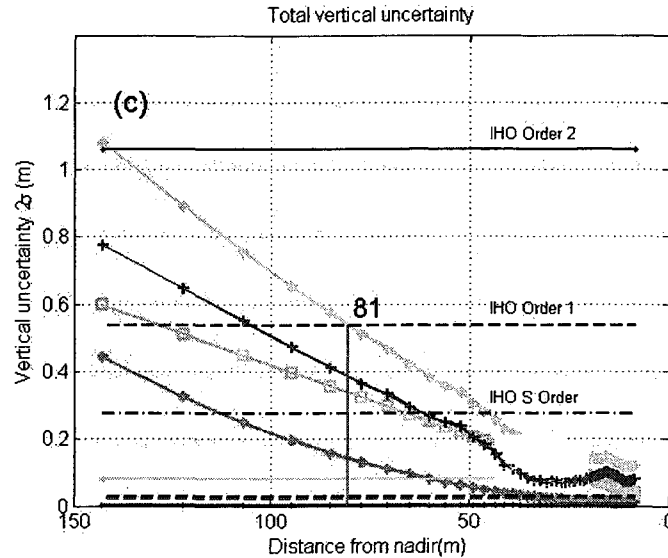


Figure 34: Theoretical total vertical uncertainty at 15-m altitude for ideal 5410 with Applanix POS M/V 320 using DGPS correctors (a), Applanix POS M/V 320 using RTK (b), and Applanix POS M/V Elite with improved sound speed profile conditions (c) showing range in predicted performance to IHO Order 1 standards out to 66 m for (a), IHO Order 1 out to 71 m for (b), and IHO Order 1 out to 81 m for (c)

NOAA frequently uses the L-3 Klein series 5000 sidescan sonar for seafloor imaging at certain range scales based on the depth below the sonar. In hull-mounted configuration on NOAA small boats, a range scale setting of 75 m is frequently used for depths less than 10-m and a range scale setting of 100 m is frequently used for depths 20-m or less. Because of the high resolution acoustic backscatter imagery and consistent object detection capability of the series 5000 and 5410 sonars, it is a reasonable assumption that if an ideal 5410 (with the modified processing code) were to be used in a hull-mounted configuration with the same range scale settings as that usually used for sidescan acquisition in depths less than 20-m, the system would acquire depth data meeting or exceeding IHO Order 2 for the entire bathymetric swath for range scale settings less than 150 m.

As shown in Table 1, NOAA usually follows a basic line spacing regimen for sidescan-only data acquisition. Lines are acquired so that the outer portion of every swath covers the nadir portion of the adjacent swath. This is referred to as a 200% coverage sidescan sonar survey. This would imply that if an ideal 5410 were used in a manner similar to the way NOAA operates a L-3 Klein series 5000 sidescan sonar, the vertical uncertainty would be greatest at nadir of each of the survey lines in a 200% sidescan sonar survey.

Range Scale (meters)	Line Spacing for Coverage	
	100%	200%
75	120	60
100	160	80

Table 1: Sidescan line spacing based on range scale and coverage

The IHO standards also include criteria for feature detection and criteria for full seafloor search. IHO Special Order and Order 1a require feature detection. No analysis was performed to determine the feature detection capability of the 5410 bathymetry, although the acoustic backscatter imagery data from the 5410 would meet the feature detection criteria. Full seafloor search is also required for IHO Special Order and Order 1a. IHO [25] defines full seafloor search as:

A systematic method of exploring the seafloor undertaken to detect most of the features (as defined by IHO); utilizing adequate detection systems, procedures and trained personnel. In practice, it is impossible to achieve 100% ensonification / 100% bathymetric coverage (the use of the terms should be discouraged).

The IHO definition does not specify that to meet the criteria for full seafloor search, the bathymetry of the entire survey must be obtained; adequate imagery can fulfill the requirement. 5410 data, acquired in the same configuration as hull-mounted L-3 Klein 5000 series sidescan sonar, would meet the requirements for full seafloor search and feature detection based solely on the acoustic backscatter imagery data.

While this study does not address feature-detection resolution of 5410 bathymetry, the bathymetry data alone could not meet the full seafloor search criteria above certain speeds. de Moustier [51] derives an equation to estimate the maximum speed to achieve complete bathymetric coverage.

$$L_N = z\varepsilon \quad (116)$$

$$T_{\min} = 2R_{\max} / c \quad (117)$$

$$V_{\max} = \frac{L_N}{T_{\min}} \quad (118)$$

Where z is the height above the bottom, ε is the along track beamwidth in radians, c is the speed of sound, R_{\max} is the maximum range, T_{\min} is the minimum time between pings, and V_{\max} is the maximum speed in m/s. Modifying these equations to reflect the 5410 (where the first bathymetry data point is at 30° from nadir, and the along track beamwidth is 0.44°).

$$L_N = 2 \tan(0.44/2) \left(\frac{z}{\cos(30)} \right) \quad (119)$$

The range scale settings for the 5410 are 50 m, 75 m, 100 m, 150 m and assuming approximate depth of operation are 5-m, 10-m, 15-m, and 20-m, the allowable speeds are presented in Table 2.

Depth	Range Scale			
	50	75	100	150
5	1.3	0.9	0.6	0.4
10	2.6	1.7	1.3	0.9
15	3.9	2.6	1.9	1.3
20	5.2	3.4	2.6	1.7
Speed (knots)				

Table 2: Maximum speed for complete bathymetric coverage

The 5410 and the L-3 Klein 5000 sidescan sonar utilize multiple beams for acoustic backscatter imagery enabling both systems to acquire sidescan sonar data at greater speeds than sidescan sonar systems not using multiple beams. The 5410 does not use multiple beams for the bathymetry. The speeds shown in Table 2 are significantly lower than the maximum speed allowable for sidescan sonar operation for the 5410 and L-3 Klein series 5000. Although the bathymetry data alone will not meet IHO requirements for full seafloor search at higher operating speeds, the combined data of the bathymetry and acoustic backscatter imagery from the 5410 do meet these criteria at higher operating speeds than those presented in Table 2 since full coverage is not required.

CHAPTER 6

CONCLUSIONS AND FUTURE WORK

6.1 Summary

An uncertainty model for an ideal 5410 was developed based on comparison of 5410 and multibeam echosounder data. This model includes angular uncertainty based on raw angle of arrival. The 5410 depth uncertainty model with all other depth uncertainties handled by the model of Hare et al. [29, 30] can be used to predict the performance of the 5410. This study has shown that an ideal 5410 could be expected to meet or exceed IHO Order 1 out to 9.5 times water depth in 15-m of water.

It should be noted that this uncertainty model is for an ideal 5410 that does not include any impact of a drifting DC bias. The assumption was made that if the drifting DC bias was resolved in the 5410 electronics, the systematic depth error in the difference data would also be eliminated. If the 5410 system used for testing were to be used for data acquisition, the systematic depth error would need to be accounted for by re-introducing the systematic artifact in the total propagated uncertainty. Similarly, if the manufacturer did not resolve the DC drift in future releases of the 5410, the systematic depth error would also need to be accounted for in any future uncertainty models. If the DC drift were

eliminated, it would also be a reasonable assumption that the angular uncertainty for the system, as a whole, would improve.

6.2 Suggestions for future work

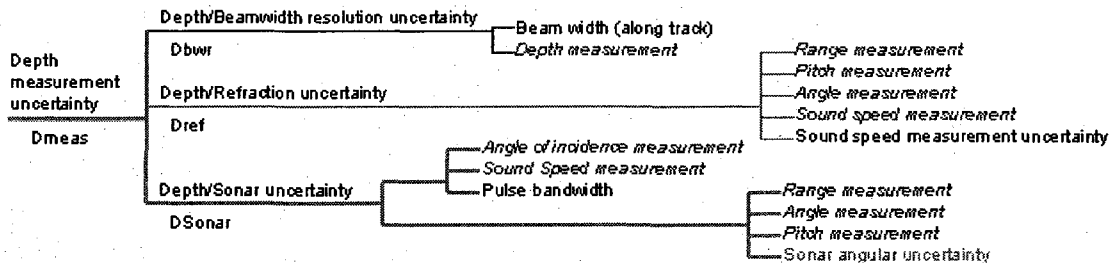
In December, 2008 a representative from L-3 Klein and UNH personnel acquired data with a 5410 version 2 aboard Coastal Surveyor. Data were acquired at different continuous wave (CW) and frequency modulated (FM) pulse settings. To date these data have not been processed. It is recommended that these data are evaluated for the following conditions:

- a) Test whether DC drift was present in the version 2 bathymetry data
- b) Test whether phase difference data shows improvement in bathymetric performance in version 2 data
- c) Test FM pulse data for bathymetric performance in version 2 data

NOTE: Significant modifications to the processing method developed by Glynn [14] will be required to process the FM bathymetric data.

If PDS system evaluations are conducted in the future, it is recommended that an intermediate step be added between testing in the tank and acquiring data underway. An approach similar to that described by Malik, et al. [52] for analysis of backscatter could also be utilized for bathymetry. Fixed mounting the sonar to a stationary location (such as a pier) with sufficient flat bottom area would have helped define the 5410 uncertainty model. Uncertainties associated with vessel motion, the motion sensor, tides, and draft would be eliminated and could be ignored during analysis, making evaluation of the sonar performance and uncertainty much clearer. Once an uncertainty model had been developed

in this manner, it could be evaluated against data acquired underway. Figure 35 shows the simplified uncertainty tree for hard mounted sonar uncertainty analysis.



After Hare et al. (1995) and Calder (2006)

Figure 35: Reduced uncertainty tree for fixed sonar (After Hare, et al. (1995) and Calder (2006))

It would be beneficial to the users of L-3 Klein series 5000 sidescan sonar data and future users of 5410 bathymetry if the version 2 were tested under both benign and challenging circumstances, mainly with and without severe thermocline conditions.

Our implementation of the 5410 GSF format should be modified to improve our dynamic range through the use of the two-way travel time scale factor, allowing thereby an extra digit to the representation of the time measurement field.

Moving beyond the empirically derived phase differencing sonar uncertainty model described in this thesis and actually implementing performance algorithms comparable to other sonar systems would help evolve the 5410 into a more robust system that is suitable for conducting hydrographic surveys that meet IHO requirements. As proposed by Hare [30] for multibeam echosounders, the ultimate goal for all PDS should be to have the system

provide an output of real-time uncertainty metrics that could be used during acquisition and recorded in the raw data, which could ultimately be used to facilitate post processing with less intervention by a hydrographer.

LIST OF REFERENCES

1. Tang, D., J. G., J. D., and K. Williams, *Analyses of high-frequency bottom and subbottom backscattering for two distinct shallow water environments*. Journal of Acoustical Society of America, 1994. **96**(5): p. 2930-2936.
2. Sintes, C., M. Legris, and B. Solaiman, *Interferometric Side Scan Sonar Signal Denoised Wavelets*, in *Proceedings of SPIE*. 2003, Independent Component Analysis, Wavelets, and Neural Networks: p.45-55.
3. Office of Coast Survey, *Field Procedures Manual*, Dept. of Commerce, Editor. 2008, NOAA. www.noaa.gov
4. Jin, G. and D. Tang, *Uncertainties of Differential Phase Estimation Associated with Interferometric Sonars*. IEEE Journal of Oceanic Engineering, 1996. **21**(1): p. 53-63.
5. Gostnell, C., *Efficacy of an interferometric sonar for hydrographic surveying: Do interferometers warrant an in-depth examination?* The Hydrographic Journal, 2005(118): p. 17-24.
6. de Moustier, C., *State of the Art in Swath Bathymetry Survey Systems*. International Hydrographic Review, 1988(2): p. 25-53.
7. Matsumoto, H., *Characteristics of SeaMarcII Phase Data*. IEEE Journal of Oceanic Engineering, 1990. **15**(4): p. 350-360.
8. Masnadi-Shirazi, M., C. de Moustier, P. Cervenka, and S. Zisk, *Differential Phase Estimation with the SeaMARC II Bathymetric Sidescan Sonar System*. IEEE Journal of Oceanic Engineering, 1992. **17**(3): p. 239-251.
9. Lurton, X. *Interferometry for bathymetry sonar: accuracy vs resolution, and a new quality estimator*. in *Proc. 5th Int. Conf. on High Resolution Survey in Shallow Water*. 2008. Portsmouth, NH: Center for Coastal and Ocean Mapping.

10. Lurton, X., *An Introduction to Underwater Acoustics Principles and Applications*. 2004, Berlin: Springer-Praxis. 18-34, 259-282, 329-330.
11. Lurton, X., *Theoretical Modeling of Acoustical Measurement Accuracy for Swath Bathymetric Sonars*. International Hydrographic Review, 2003. 4(2): p. 17-30.
12. Lurton, X., *Swath Bathymetry using Phase Difference: Theoretical Analysis of Acoustical Measurement Precision*. IEEE Journal of Oceanic Engineering, 2000. 25(3): p. 351-363.
13. Glynn, J., C. de Moustier, and L. Huff, *Survey operations and results using a Klein 5410 bathymetric sidescan sonar*, in *U.S. Hydro*. 2007: Norfolk, VA.
14. Glynn, J., *Acoustic calibration and bathymetric processing with a Klein 5410 side scan sonar*, in *MS Thesis*. 2007, University of New Hampshire: Durham.
15. Denbigh, P.N., *Signal Processing Strategies for a Bathymetric Sidescan Sonar*. IEEE Journal of Oceanic Engineering, 1994. 19(3): p. 382-390.
16. Denbigh, P.N., *Swath Bathymetry : Principals of Operation and an Analysis of Errors*. IEEE Journal of Oceanic Engineering, 1989. 14(4): p. 289-298.
17. de Moustier, C., P. Lonsdale, and A. Shor, *Simultaneous Operation of the Sea Beam Multibeam Echo-Sounder and the SeaMARCII bathymetric Sidescan Sonar System*. IEEE Journal of Oceanic Engineering, 1990. 15(2): p. 84-94.
18. de Moustier, C., *Signal Processing for Swath Bathymetry and Concurrent Seafloor Acoustic Imaging*. 1993, Kluwer Academic Publishers in cooperation with NATO Scientific Affairs Division: p.328-354.
19. Bird, J.S. and G. Mullins, *Analysis of Swath Bathymetry Sonar Accuracy*. IEEE Journal of Oceanic Engineering, 2005. 30(2): p. 372-390.

20. Bird, J. and G. Mullins, *Bathymetric Sidescan Sonar Bottom Estimation Accuracy: Tilt Angles and Waveforms*. IEEE Journal of Oceanic Engineering, 2008. **33**(3): p. 302-320.
21. Cervenka, P. and C. de Moustier, *Postprocessing and Corrections of Bathymetry Derived from Sidescan Sonar Systems: Application with SEAMARC II*. IEEE Journal of Oceanic Engineering, 1994. **19**(4): p. 619-629.
22. le Clerc, F., *Performance of Angle Estimation Methods Applied to Multibeam Swath Bathymetry*, in *Oceans 1994*. 1994: Brest, France: p. 231-236.
23. Office of Coast Survey, *NOAA Hydrographic Surveys Specifications and Deliverables*, Dept. of Commerce, Editor. 2008, NOAA. www.noaa.gov
24. *L-3 Klein system 5000 brochure*. 2008, L-3 Klein. p. 2. www.l-3klein.com
25. International Hydrographic Organization, *Special Publication no.44 IHO Standards for Hydrographic Surveys*. 5th ed. 2008, Monaco: International Hydrographic Bureau. www.iho-ohi.net
26. Zerr, B., S. Le Goanvic, B. Le Bretton, and C. Genty, *Bathymetric Sidescan Sonar : a System Dedicated to Rapid Environment Assesment*. Oceans 2005 - Europe, 2005. **1**(20-23): p. 118-123.
27. Caris, *Hips and SIPS 6.1 users guide*, www.caris.com, Editor. 2007.
28. Calder, B. and A. McLeod, *Ultraprecise Absolute Time Synchronization for Distributed Acquisition Systems*. IEEE Journal of Oceanic Engineering, 2007. **32**(4): p. 772-785.
29. Hare, R., Godin, A., Mayer L., *Accuracy estimation of Canadian Swath (multibeam) and Sweep (multi-transducer) Sounding Systems in Tech. Rep.* 1995, Canadian Hydrographic Service and University of New Brunswick: Ocean Mapping Group.
30. Hare, R., *Error Budget Analysis for US Naval Oceanographic Office (NAVOCEANO) Hydrographic Survey Systems*, in *Tech. Rep.*, Naval

Oceanographic Office, Editor. 2001, University of Southern Mississippi Hydrographic Science Research Center (HSRC).

31. Gostnell, C., J. Yoos, and S. Brodet, *NOAA test and evaluation of phase differencing bathymetric sonar technology*, in *Canadian Hydrographic Conference*. 2006: Halifax, Nova Scotia, Canada: p. 1-8.
32. Hogarth, P., *Achieving high accuracy using wide swath bathymetry systems*, in www.geoacoustics.com/. 2002, GeoAcoustics, Ltd.
33. Hiller, R., Calder, B.R., Hogarth, P., Gee, L. *Adapting CUBE for phase measuring bathymetric sonars*. in *4th international conference on high-resolution survey in shallow water*. 2005. Plymouth, Devon, UK.
34. Calder, B. and L. Mayer, *Automatic processing of high-density, high-rate multibeam echosounder data*. *Geochemistry Geophysics Geosystems*, 2003. **4**(6): p. 1-22.
35. Tait, P.G., *A treatise on dynamics of a particle with numerous examples*. 1900, New York: Macmillan Company.
36. Bryan, G.H., *Stability in aviation, an introduction to dynamical stability as applied to the motions of aeroplanes*. 1911, Boston: Macmillan and Company.
37. Goldstein, H., *Classical Mechanics*. Second ed. 1980, Reading: Addison-Wesley.
38. Glang, G. and R. Brennan, *WHITING Hydrographic Survey H11014*, NOAA, Editor. 2001, www.ngdc.noaa.gov/mgg/bathymetry/hydro.html.
39. Brennan, R.T., *An uncertainty model for the tidal constituent and residual interpolation (TCARI) method of water level correction*, in *MS Thesis*. 2005, University of New Hampshire: Durham. p. 90.
40. Clay, C. and H. Medwin, *Acoustical oceanography*. 1977, New York: John Wiley & Sons: p. 271.

41. Huff, L. and R. Becker. *Microcomputer program for processing and management of NOS sound velocity data*. in *Mar. Tech. Soc. Conf. on Marine Data Systems*. 1989. New Orleans, LA.
42. de Moustier, C., *Angle of Incidence computation*. 2008: Lecture notes, Durham, NH.
43. Applanix, *POS MV v4 installation and operation guide*, www.applanix.com, Editor. 2005: Richmond Hill, Ontario, Canada.
44. Caris. *Manufacturer accuracy values for total propagated error computation*. 2008 [cited; Available from: <http://www.caris.com/TPE/>].
45. L-3 Klein, *Series 5000 sonar operations and maintenance manual*. 2004, L-3 Communications: Salem, New Hampshire: p. I-4 - I-9, C-2 - C-4, D4.
46. Hughes Clarke, J., *Dynamic motion residuals in swath sonar data: ironing out the creases*. *International Hydrographic Review*, 2003: p. 1-30.
47. Dieck, R.H., *Measurement Uncertainty Methods and Applications*. 4th ed. 2007, Research Triangle Park: ISA - The Instruments, Symptoms, and Automation Society: p. 11-14, 24-26, 114-124, 186.
48. Ward, L.G., *Sedimentology of the lower Great Bay/Piscataqua River Estuary*, N.R.D.R. Department of the Navy, San Diego, California. (UNH CMB/JEL Contribution Series Number 314), Tech. Rep., Editor. 1995. p. 102.
49. Hammerstad, E., *Comments on improved Simrad EM series error models*, *Tech. Rep.* 1995.
50. SAIC, *Generic Sensor Format Specification*. 2008, Naval Oceanographic Office.
51. de Moustier, C., *Sidescan Sonar Methods*, in *Fundamentals of Ocean Mapping* in Lecture notes. 2007, UNH: Durham, NH.

52. Malik, M., L. Mayer, L. Fonseca, L. Ward, L. Huff, and B. Calder, *Approaches and requirements of quantitative comparison of the multibeam sonar benthic acoustic backscatter*, in *Proc. 5th Int. Conf. on High Resolution Survey in Shallow Water*. 2008, CCOM: Portsmouth, NH.
53. Becker, R. and P. Grim. *Sound velocity products for NOS hydrography*. in *Proceedings from the Canadian Hydrographic Conference*. 1989. Vancouver, BC, Canada.
54. Urick, R., *Principles of underwater sound*. 3rd ed. 1983, Los Altos, California: Peninsula publishing.
55. Ainslie, M. and J. McColm, *A simplified formula for viscous and chemical absorption in sea water*. Acoustical Society of America, 1998. **100**(3): p. 2.

APPENDIX A

LIST OF SYMBOLS

α	absorption coefficient	(dB loss/m)
α_i	absorption coefficient for layer i	(dB loss/m)
a	fixed heave uncertainty	(m)
b	heave (% total heave) uncertainty	
BW	bandwidth	(kHz)
c	speed of sound	(m/s)
c_i	speed of sound at layer i	(m/s)
c_{Sensor}	speed of sound at sensor	(m/s)
cp	speed of sound profile	(m/s vs m)
c_{ray}	harmonic speed of sound for ray	(m/s)
d	element spacing	(m)
Ds	static draft (positive out of water)	(m)
Dd	dynamic draft (positive into water)	(m)
E	Easting	(m)
ϵ	beamwidth	($^\circ$)
f	frequency	(Hz)
g	sound speed gradient	(seconds ⁻¹)
g_i	sound speed gradient at layer i	(seconds ⁻¹)
γ	grid resolution	(m)
Γ	pitch (positive bow up)	($^\circ$)
Γ_{att}	pitch from attitude sensor	($^\circ$)
Γ_{bias}	pitch bias	($^\circ$)
Γ_{meas}	pitch measurement uncertainty	(radians)
H	heave (positive out of water)	(m)
H_{att}	heave from attitude sensor	(m)
H_{ind}	induced heave	(m)
ρ	ray parameter	(s/m)
Ψ	roll (positive port up)	($^\circ$)
Ψ_{att}	roll from attitude sensor	($^\circ$)
Ψ_{bias}	roll bias	($^\circ$)
Ψ_{meas}	roll measurement uncertainty	(radians)
r	radius or range	(m)
r_{est}	estimated range of sounding	(m)
r_h	horizontal range	(m)
r_{hi}	horizontal distance for layer I	(m)
r_{hr}	horizontal distance for partial layer	(m)
R	radius of curvature	(m)
R_i	radius of curvature for layer i	(m)
R_r	radius of curvature for partial layer	(m)
Δr_s	range sample distance	(m)
s	distance traveled	(m)
s_i	distance traveled for layer i	(m)
τ	pulse duration	(s)
S	salinity	(PSU)
S_i	salinity for layer i	(PSU)

T	temperature	(°C)
T_i	temperature for layer i	(°C)
t	time	(s)
t_r	recorded two way travel time	(s)
t_i	travel time for layer i	(s)
t_r	remaining travel time	(s)
Tides	height of tides above MLLW	(m)
ϕ_{AB}	phase difference between elements A and B	(radians)
Φ	yaw (azimuth orientation, positive clockwise)	(°)
Φ_{att}	yaw from attitude sensor	(°)
Φ_{bias}	yaw bias	(°)
Φ_{meas}	yaw measurement uncertainty	(radians)
θ	angle of arrival	(°)
θ_{Bore}	angle from broadside of transducer (boresight)	(°)
θ_{Down}	mounting angle of transducer with respect to horizontal	(°)
θ_{error}	calculated angular error	(°)
θ_i	angle of incidence for layer i	(°)
θ_N	angle of incidence for last complete layer	(°)
θ_r	angle of incidence for bottom	(°)
θ_{Raw}	angle of arrival (raw)	(°)
θ_{Corr}	angle of arrival (corrected for roll and pitch)	(°)
θ_{est}	estimated bearing of sounding	(°)
λ	wavelength	(m)
N	Northing	(m)
X	installation athwartships offset (positive to starboard)	(m)
Y	installation fore-aft offset (positive forward)	(m)
Z	depth below sensor	(m)
Z_{Diff}	depth difference between surface and sounding	(m)
ΔZ_i	depth difference of layer i	(m)
Z_{red}	reduced sensor depth	(m)
Z_{sensor}	depth of sensor	(m)
Z	installation vertical offset (positive down)	(m)

APPENDIX B

UNCERTAINTY SCENARIO

Depth	5 m or 20 m
Sound speed	1500 m/s (zero gradient)
Maximum Roll	3°
Maximum Pitch	3°
Maximum Range Scale	150 m
Maximum (measured) Heave	0.5 m
Usable Angular sector	30° to 90°
CW Pulse duration	176×10^{-6} s
Bottom	Flat

APPENDIX C

SONAR UNCERTAINTY VALUES

Element spacing (λ) port/stbd	2.48/3.90/6.38 [14] / 2.41/4.00/6.41 [14]	
Down angle	20°[14]	
Maximum number of soundings	up to 5000 depending on range scale	
Operating frequency	455 kHz[14]	
Maximum angle from nadir	90° [14]	
Beamwidth across track	0.4° (estimate)	
Beamwidth along track	0.4° (estimate)	
Steering angle	not applicable, no beam steering	
Range sampling frequency	22750 Hz [14]	
Minimum pulse duration	132 μ s CW [14]	176 μ s CW [14]
Bandwidth (132 /176 μ s CW)	6.3 kHz [14]	4.8 kHz [14]
Range sampling resolution (132 /176 μ s CW)	0.120 m [14]	0.156 m [14]

NON-SONAR UNCERTAINTY VALUES

Applanix POS M/V 320 with RTK correctors (2m baseline)

Navigation	0.10 m[44]	Heading	0.01° [44]
Heave % amplitude	5 [44]	Heave	0.05 m[44]
Roll and Pitch	0.01° [44]		

Sound speed measurement uncertainty	1 m/s (estimate)
Surface sound speed measurement uncertainty	1 m/s (estimate)
Tide measurement uncertainty	0.005 m (estimate)
Tide zoning uncertainty	0.01 m (estimate)
Speed over ground	0.01 m/s (estimate)
Loading	0.01 m (estimate)
Static draft	0.005 m (estimate)
Dynamic draft	0.01 m (estimate)
Y Offset	9.276 m (measured)
X Offset (port/starboard)	- 0.084 m / 0.084 m (measured)
Z Offset	1.53 m (measured))
Pitch Bias (port/starboard)	1° / 1° (calculated)
Roll Bias (port/starboard)	-2.4° /-3.6° (calculated)

APPENDIX D

COMMENTS ON SOUND SPEED PROFILE VARIABILITY

Sound speed casts acquired during this project to complement 5410 data acquisition showed great variability throughout the experiment. The greatest variability in sound speed profiles were observed in the dataset acquired in the summer (day of the year, DOY 211 to 219) over the reference surface area. Those casts showed large variations over time in temperature (up to 13°C) and sound speed (up to 39 m/s) from the surface to the lowest measured points (maximum measured depth was 25.5 m). In the vicinity of casts acquired over the reference surface area in the summer, the surface waters gradually warmed throughout the day and apparently cooled overnight. The first few casts on DOY 211 (summer days) were acquired in the Piscataqua River and in Portsmouth Harbor. The casts acquired on DOY 275, 276, and 277 (autumn days) were acquired in Portsmouth Harbor. Figures 36 and 37 incorporate the deepest sound speed points which were extrapolated by Velocwin [53]. Strong negative gradient multipath artifacts were observed in both the acoustic backscatter imagery and bathymetry data in the presence of a strong thermocline at range scales greater than 50 m. Figure 36 shows a compilation of sound speed casts extended by Velocwin for different days of acquisition. For those sound speed casts with a well defined thermocline, the depth of the thermocline gradually deepened as each day progressed.

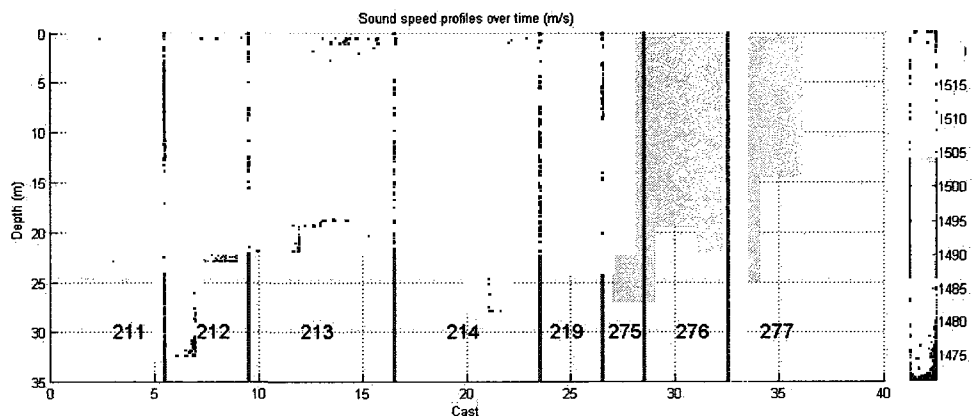


Figure 36: Sound speed cast compilation where the DOY of the cast is shown in the graph at a depth of 30 m

Figure 37 shows plots of sound speed, temperature, and salinity for all the acquired casts.

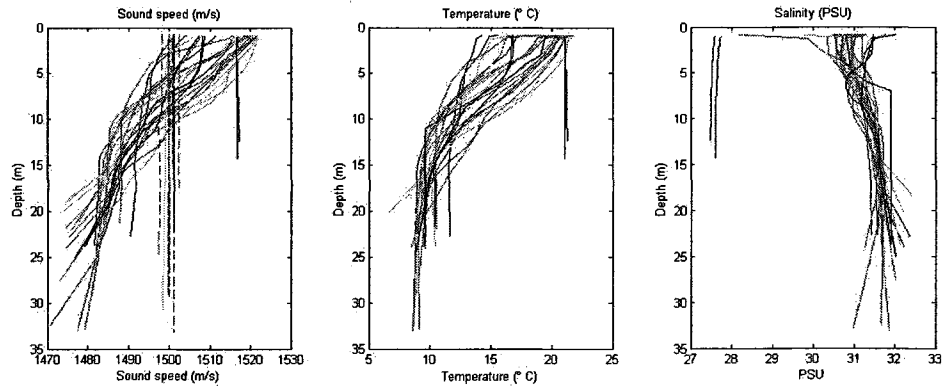


Figure 37: Sound speed, temperature, and salinity of casts. Deepest points of each salinity and temperature profiles were extrapolated

Figure 38 shows an example of negative sound speed gradient causing multipath artifacts in the acoustic backscatter imagery. The apparent structure on the right side of the image are the artifacts and do not represent the true bottom.

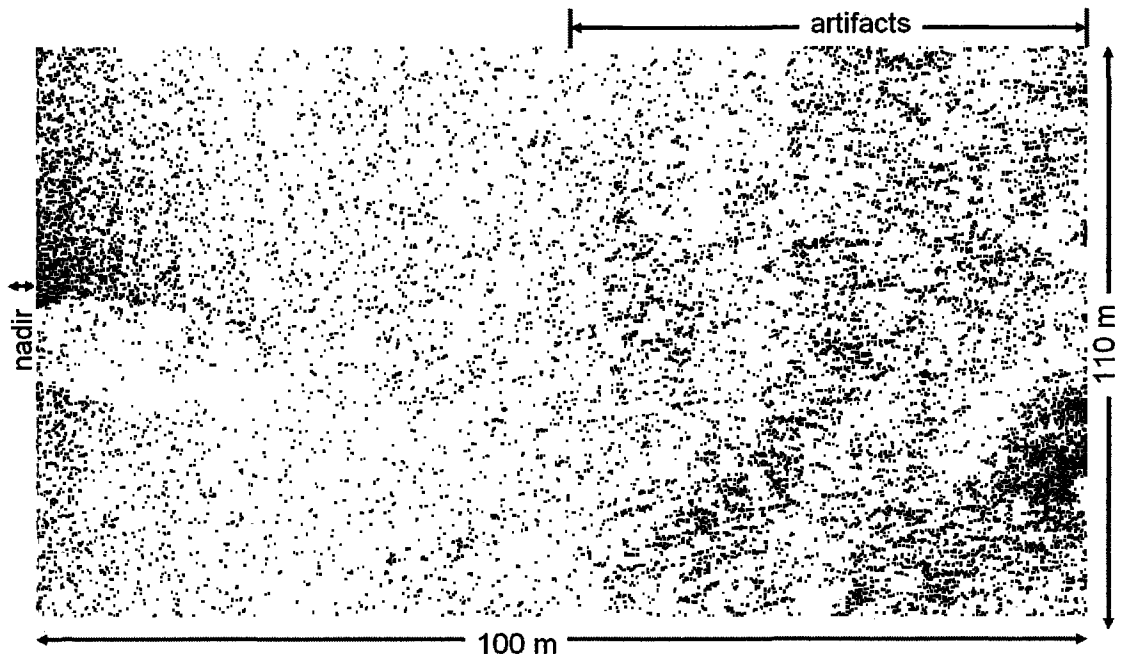


Figure 38: Acoustic backscatter negative sound speed profile gradient multipath interference for the starboard side out to 100 m. The left is nadir and the right is the farthest away from the sonar. The wavy structures to the right are due to interference, (DOY 213 in Figure 36)

APPENDIX E

SONAR EQUATIONS

The sonar equations can be used to describe the data and to estimate sonar uncertainty. Although the equations derived in [9, 11, 12, 30] were not used in this thesis for 5410 uncertainty, the signal to noise ratio that can be calculated from the magnitude product described in Appendix E could become useful in future versions of the 5410. As shown by Urick [54] the sonar equation for seafloor echo-sounding is:

$$EN = SL - 2TL + BSL - NL + DI_R \quad (120)$$

Where EN is the echo level, TL is the transmission loss, BSL is the backscattered level, NL is the noise level, and DI_R is the receive directivity index. The echo level for any given element pair and ping can be directly calculated using the real (I) and imaginary (Q) components of the element.

Time varied gain (TVG) was applied during acquisition, and was removed from the magnitude product in order to examine the equivalent raw signal return. Appendix E presents the raw signal return in a “water fall” format.

The gain applied during acquisition is composed of a fixed gain value and TVG. The fixed gain is user selected and recorded in the raw data file in the header as ‘tvg page’ [45]. The TVG is calculated by using the distance traveled (s) and the absorption coefficient (α) expressed in equation (120). The absorption coefficient used by Klein was 0.1 dB/m (Parent, 2009, Personal Communication).

$$TVG = 30 \log_{10}(s) + 2\alpha \times s \quad (121)$$

TVG can also be considered as a time dependant correction.

$$tv_g = \left[\frac{c \times t_f}{2} \right]^3 10^{\left(\frac{2\alpha(c \times t_f)/2}{10} \right)} \quad (122)$$

The measured receive beam pattern (Bp) shown in Figure 39 from Glynn [14] was applied to the equivalent raw magnitude values.

$$M = (M_r - Bp) / tv_g \quad (123)$$

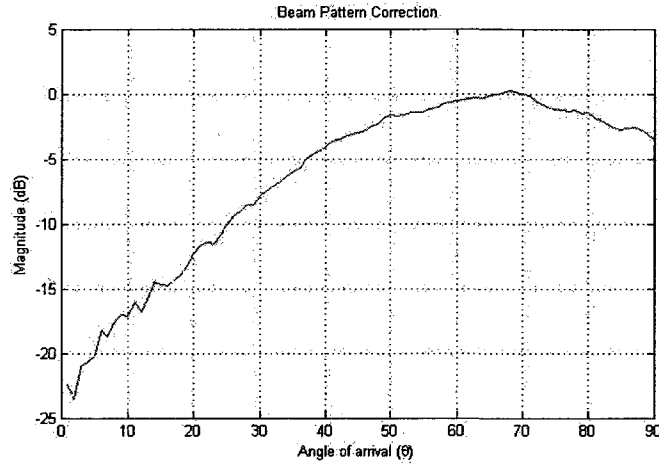


Figure 39: Receive beam pattern correction (from Glynn, 2007)

Ainslie and McColm [55] describes the calculation of total absorption as:

$$\alpha = \left(\frac{A_1 f_1}{f_1^2 + f^2} + \frac{A_2 f_2}{f_2^2 + f^2} + A_3 \right) f^2 \quad (124)$$

Where the frequency (f) is in kHz, the temperature (T) is in °C, the salinity (S) in ppm, and depth (z) in km.

$$f_1 = 0.78 \sqrt{S/35} \exp^{(T/27)} \quad (125)$$

$$f_2 = 42 \exp^{(T/17)} \quad (126)$$

$$A_1 = 0.106 \exp^{[(pH-8)/0.56]} \quad (127)$$

$$A_2 = 0.52(1 + T/43)(S/35) \exp^{-z/6} \quad (128)$$

$$A_3 = 4.9 \times 10^{-4} \exp^{(-T/27 - z/17)} \quad (129)$$

Not only can the signal to noise ratio for 5410 data be used for uncertainty analysis, but also for a second version of acoustic backscatter imagery. Like the bathymetry, the acoustic backscatter imagery does not use multiple focused beams, but does have the advantage of being completely georeferenced. Solving for the backscatter level (BSL) in equation (120) would provide lower resolution acoustic backscatter that could be used to augment the focused multibeam acoustic backscatter imagery.

APPENDIX F

PLOT OF MAGNITUDE OUTPUT (SINGLE LINE, 1 MIN OF DATA)

The Glynn [14] example shows that the quadrature sampled vectors B1 and B2 produced by two separate elements in the 5410 are described as:

$$B1 = I_1 + jQ_1 = M_1 e^{j\phi_1} \quad (130)$$

$$B2 = I_2 + jQ_2 = M_2 e^{j\phi_2} \quad (131)$$

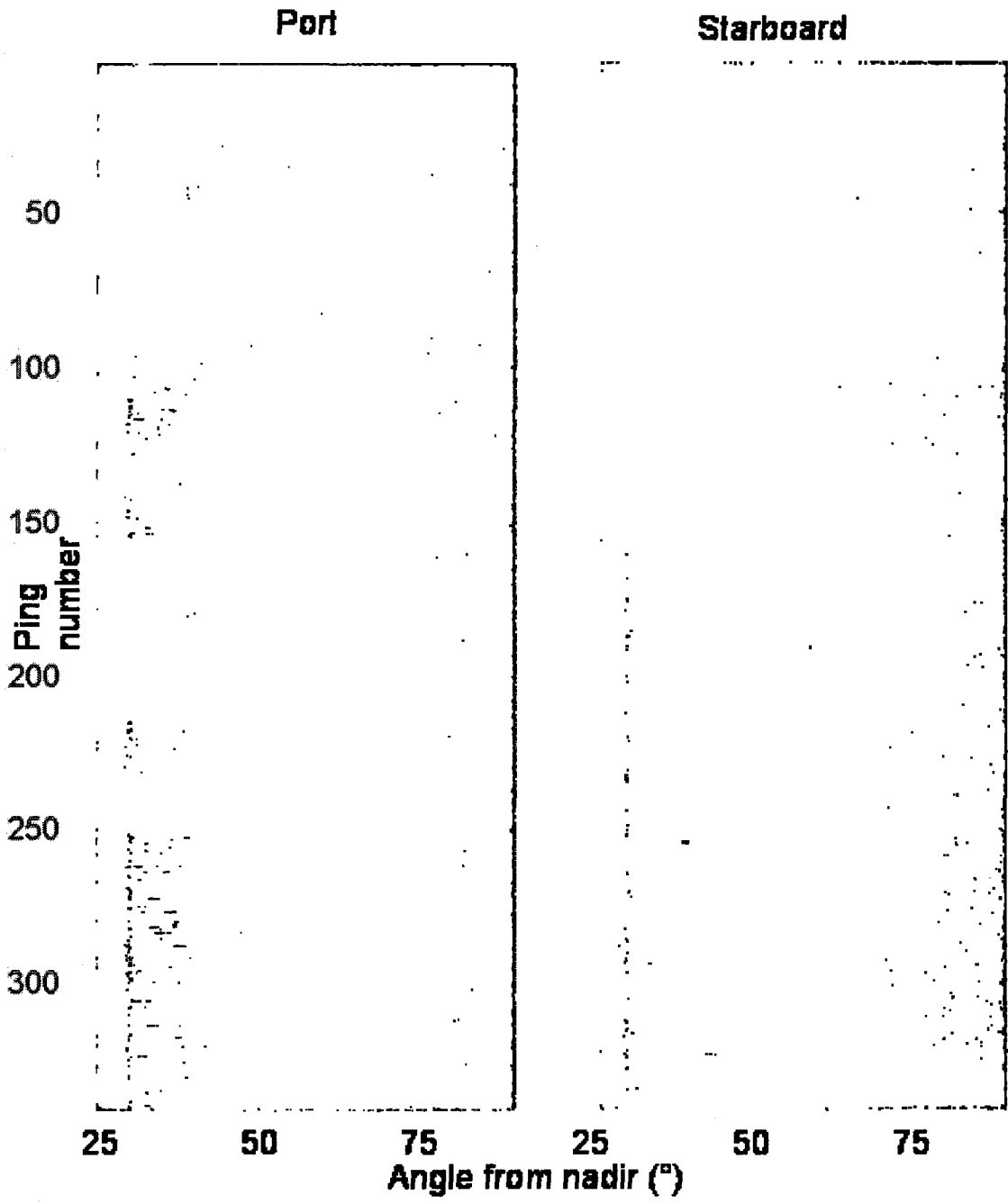
Where the complex conjugate of B1 is:

$$B1^* = I_1 - jQ_1 = M_1 e^{-j\phi_1} \quad (132)$$

The product of B2 and B1* is shown:

$$B2B1^* = (I_2 + jQ_2)(I_1 - jQ_1) = M_1 M_2 e^{j(\phi_2 - \phi_1)} \quad (133)$$

The resulting vector averaged magnitude from the three element pairs is plotted below with tvg removed.



APPENDIX G

NARRATIVE OF MAJOR POINTS

Acquisition

- 1) Acquire reference surface multibeam echosounder data over different bottom types and depths.
- 2) Acquire data with the sonar to be examined over same area. As much as possible reduce non-sonar uncertainties.

Processing

- 1) Process multibeam echosounder data in CARIS HIPS and generate CUBE surfaces, exporting the depth, uncertainty, and position of each grid node to a text file.
- 2) Process sonar data to be examined in Matlab
- 3) Tag each sonar sounding with reference surface depth, uncertainty, and range to grid node.
- 4) Calculate uncertainty for each sonar sounding except for sonar uncertainties
- 5) Solve for sonar uncertainties

The analysis described in this thesis could have been improved by utilizing the reference surface node uncertainty and sounding distance from each node so the difference data could be weighted (in effect, weighing reference surface nodes with higher uncertainty less than those with less uncertainty). In this way, the uncertainties associated with the multibeam echosounder would have a minimal impact on the solution of the sonar uncertainties.

As mentioned in chapter 6, data acquisition of the sonar while fixed would be an appropriate step before underway data acquisition.

Recommendations for future work:

- 1) Use smoothed best estimate (SBET) export for uncertainty calculations for attitude sensor rather than static uncertainty values provided by vendor.
- 2) Solve for sonar biases in CARIS HIPS, but omit processing remaining sonar data under analysis in CARIS HIPS before exporting to Matlab. Process raw data in Matlab and only process the reference surface multibeam echosounder data in CARIS HIPS to create a CUBE surface. The ray tracing method described in the thesis would have to be slightly modified so the position of each sounding is calculated in Matlab.

- 3) Even if the sonar being evaluated doesn't require a surface sound speed measurement in real time, it is recommended that those data be recorded and time tagged to allow for use in ray tracing if necessary.
- 4) The CARIS HIPS dump raw export tools don't always export all data from a raw data file; depending on the format it may be necessary to write a binary reader for a given raw data format.
- 5) The following group messages were recorded in the POS M/V ethernet log file: 1, 2, 3, 4, 5, 9, 10, 99, 102, 110, 111, 113, 114, 10006, 10009, 10011, 10012. These groups required use of an exporter written by Calder to export the attitude from the ethernet log file to a text format which was imported into Matlab

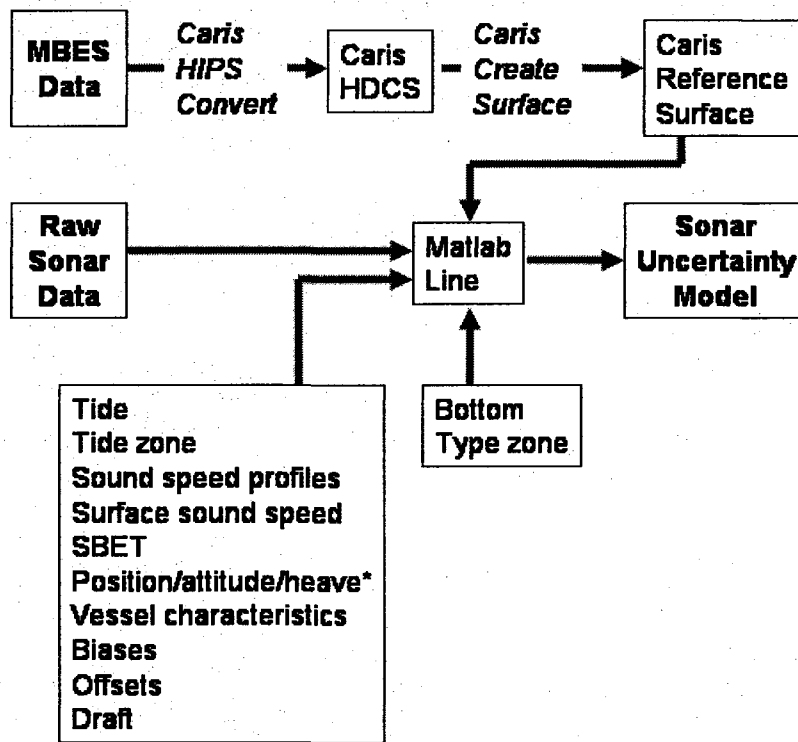


Figure 40: Flowchart of proposed processing steps to solve for sonar uncertainties using multibeam echosounder (MBES) data as a reference surface